Numerical Simulation of Transverse Jet Injection into a Supersonic Crossflow

M.Tech Dissertation
by

Tanisha Kishor Joshi
(Roll No. 183010025)

Guide:
Dr Krishnendu Sinha

Department of Aerospace Engineering
Indian Institute of Technology Bombay
Mumbai 400076 (India)

June 2020

Certificate

Department of Aerospace Engineering

Indian Institute of Technology, Bombay

Certified that this dissertation titled **“Numerical Simulation of Transverse Jet Injection into a Supersonic Crossflow”** by **Tanisha Kishor Joshi (Roll No. 183010025)** is approved for the degree of Master of Technology in Aerospace Engineering. Certified further that, to the best of our knowledge, the report represents work carried out by the student.

Examiner

Examiner

Date: June 2020

Guide : Dr Krishnendu Sinha

Declaration

I, the undersigned, hereby declare that I am the sole author of this dissertation. To the best of my knowledge, this dissertation contains no material previously published by any other person except where due acknowledgement has been made and relevant sources have been cited.

Tanisha

Date: June 2020

Tanisha Kishor Joshi

Acknowledgements

I wish to express my sincere gratitude to my guide, Professor Krishnendu Sinha under whom it has been a wonderful learning experience. I would also like to thank Jagadish, Pratik, Subhajit, Harsha, Pranav, Yogesh, Rachit and Mukesh from the HCFD Lab , IIT Bombay. It is because of their valuable support and inputs,that I am able to complete and present my dissertation.

Abstract

An underexpanded sonic jet, when injected perpendicularly into a supersonic cross-flow, gives rise to a complex flow-field characterised by shocks, recirculation zones, supersonic and subsonic pockets and curved shear layers. The report presents an attempt that has been made to capture these features using the Wilcox standard k-w turbulence model, and its Shock Unsteadiness (SU) modified form; with an implicit Steger-Warming scheme for computation. Such simulations are important in the development of scramjet combustors as well as in thrust vectoring of supersonic aircraft. Besides that, the simple geometry but complex flow field of the problem makes it a good candidate to assess the behaviour of different turbulence models at high flow speeds. The flow physics has been explained first, followed by a review of the existing literature data for both two dimensional as well as three dimensional injection. Next, the mathematical model is outlined, where the numerical scheme and discretisation methods are summarised. A gist of the Shock Unsteadiness Model developed by Sinha et al.[1] is also presented. Simulations are performed for a transverse 2D injection of a jet into a freestream of Mach 3.75 through a 1mm wide slot. The experimental cases of Aso et al[3] are taken as reference. The simulations are performed using both, the standard and SU modified $k - \omega$ models. An attempt is made to further modify the SU model to get some improvements. Finally, comparisons are made between our results, experimental data and simulation results available in literature.

Table of Contents

List of Figures

List of Tables

Chapter 1

Introduction

1.1 Significance of Study

The injection of a sonic jet into a supersonic cross-flow is seen in processes like fuel injection into scramjet combustors and thrust vectoring of supersonic aircraft and rockets. The resulting flow field consists of complex flow features; the formation of which has been explained in the upcoming section. It becomes essential to numerically predict such features with a fairly good accuracy in order to determine their sensitivity to the geometric design and also the extent of mixing and penetration of the jet. Further, the problem has simple geometric requirements but complicated flow structure. This makes it a good choice to test the behaviour of different turbulence models at high flow speeds.

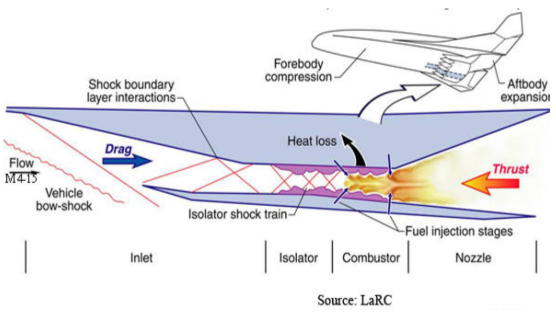

(a) Scramjet Combustors

(b) Thrust Vectoring

Figure 1.1: Applications of jet injection into a supersonic cross-flow

1.2 Flow Features

1.2.1 2-D Flow Features

When a jet is injected through a slot whose width is small compared to its span, the flow field can be approximated as a two-dimensional case. The flow features arising from such an injection is as shown in Figure 1.2. The injected jet, being under-expanded, expands into the cross-flow but is simultaneously deflected downstream by it. The cross flow, on the other hand, sees this jet as an obstruction - this leads to the formation of a bow shock just upstream of the injection slot. Due to this strong jet induced bow shock, the incoming boundary layer is subjected to a high adverse pressure gradient causing it to separate and form a recirculation bubble. Typically, there are two-three vortices seen within this bubble, termed as primary/secondary/ tertiary upstream vortices (PUV/SUV/TUV) based on their relative sizes. There is also a separation shock present before the bow shock as a result of this recirculation zone. The bow shock and the separation shock create a shock pattern known as the lambda shock which can be visualized from the red line in Figure 1.3. Post bow-shock we have the free shear layer of the jet curving into the flow. The expansion fans arising within the under-expanded jet hit the jet boundary and reflect as compression waves. These compression waves merge and create a barrel-shock inside the jet boundary. This is shown in Figure

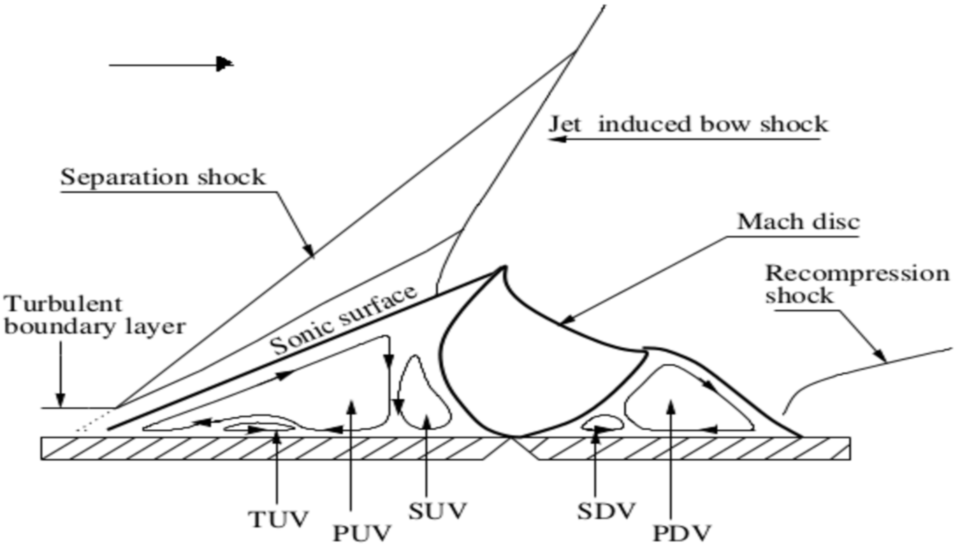

Figure 1.2: Flow field resulting from two-dimensional injection of jet through a slot into a supersonic cross flow[4]

1.3. This barrel shock is terminated by a Mach disk. The Mach disc is basically a normal shock like structure which will be seen as a plane in two-dimensional flow and a circular disc in three-dimensional flow. Downstream of the jet, there is again a recirculation zone with two (primary and secondary) downstream vortices (PDV/SDV). The supersonic flow over the downstream recirculation zone needs to turn at the end of this bubble, this occurs by the formation of a reattachment shock. The vortices (upstream as well as downstream) have a more complex structure in the three dimensional flow, this is elaborated in the next section.

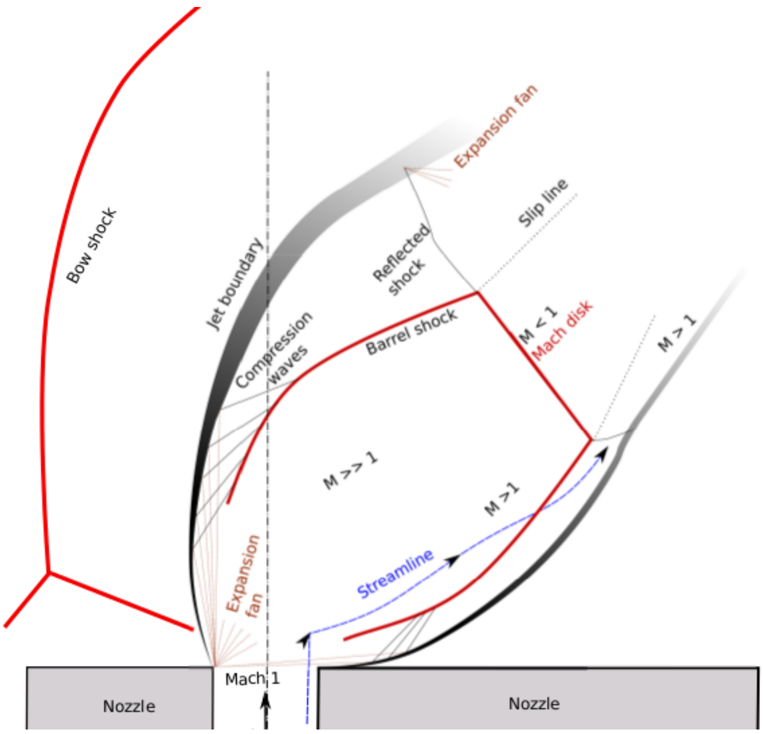

Figure 1.3: Barrel shock formation within the jet boundary

1.2.2 3-D Flow Features

The three-dimensional flow structure of the jet is shown in Figure 1.4. Due to the effect of three dimensionality braught in by a circular hole injection, there are several flow features observed in this case which are not seen in the 2D experiments/simulations. Firstly, there is no reattachment shock seen downstream of the jet; rather, the jet develops into a kidney shaped structure which is essentially a pair of counter rotating vortices. This is formed because the pressure above the jet- post bow shock, is higher than that downstream of the jet. Due to the three dimensionality, the flow has space to spill over and move beneath the jet, thus creating the counter rotating vortices. Below these vortices, there is a complex nested region of recirculating flows. The downstream vortices do not have their axis perpendicular to the flow, unlike the 2D case. The bow shock too, is curved around the jet.

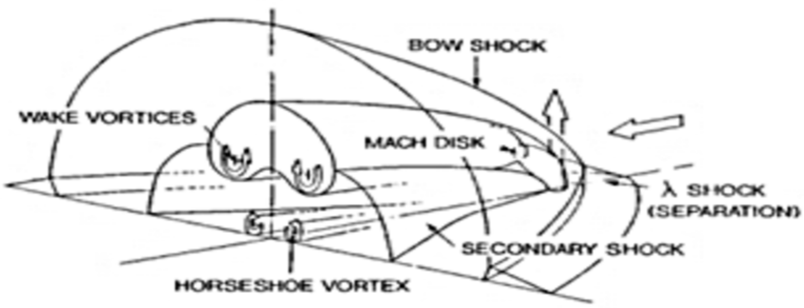

Figure 1.4: Horseshoe vortices and curved bow shocks due to three dimensionality of flow[23]

1.3 Focus of Study

In our current project, we have focused on accurately predicting the size of the separation bubble formed upstream of the injector. This is essential to study because the separated,recirculating region traps the injected gases (fuel) which leads to more fuel residence time, larger release of combustion energy and high heat transfer rates near the injector.

1.4 Summary

Injecting an under-expanded sonic jet into a supersonic cross-flow leads to the formation of an interesting flow structure comprising of strong bow shocks, recirculation zones, curved shear layers, horse-shoe vortices, subsonic pockets, barrel shock and Mach disc. Understanding the underlying physics and accurately predicting the flow features of such problems is essential for applications such as scramjet combustors, supersonic thrust vectoring and development of high speed turbulence models. In case of fuel injection into combustors, the size of the upstream separation bubble plays an important role in determining the fuel mixing and heat transfer rates.

Chapter 2

Literature Review

There are several experiments that have been conducted in the past for 2D and 3D cases. They are the main sources of validating the results of numerical simulations. The primary challenge in getting experimental data is that the supersonic flow structure is highly susceptible to minute changes in the geometry and flow conditions, thus, care must be taken that the measuring instruments cause minimum interference with the actual flow. Hence, most experiments give data of the wall static pressure distribution. Recent development in measurement systems such as Laser Doppler Velocimetry (LDV) and Mie scattering has made interior flow field data available. The results computed in this study are compared with the slot injection experiments of Aso et. al[3]

Previously, simulations have been conducted using k-epsilon, k-omega and RTSM turbulence models coupled with various types of corrections and numerical schemes. The simulations run as a part of this project are done using the Wilcox standard k-ω turbulence model and an implicit Steger Warming method for flux prediction. Comparison of results from all available simulation models helps us evaluate their behaviour and utility better.

2.1 Experiments

2.1.1 2-D Slot Injection

The work of Spaid and Zukoski[12] tried to eliminate the three dimensionality effects in slot injection experiments and determine the influence of parameters such as Mach number, pressure ratio, and injectant gas composition on the two-dimensional flow field. Out of the experimental data sets available, this one is valuable since it has minimum three dimensionality effects, provides data over a large range of injection pressure ratios and a good spatial resolution of wall pressure data. Some analytical calculations for the effective thrust force were also done.

A paper by Hawk and Amik[10] attempts to unify some of the available data by means of a relatively simple inviscid dimensionless parameter - the momentum flux ratio. They found a good amount of correlation between the flow geometry features and the momentum flux ratio for a constant free stream Mach number and Reynold's number.

Aso et al.[3] conducted experiments where a gaseous nitrogen jet is injected normally into the external flow of Mach 3.75 through a transverse slot nozzle mounted on a flat plate model. The total pressure of the freestream was 1.2MPa and the Reynolds number was $2x10^7$. The experiments were conducted with different widths of the slot and varying total pressure ratios of the jet to the free stream. The experimental setup was similar to that of Spaid and Zukoski.[12] Table 2.1 summarises the geometry and flow conditions used in the experiments. The

Table 2.1: Aso's experimental conditions

Freestream Mach	M_∞	3.75
Freestream Total Temperature	To_∞	283-299 K
Freestream Total Pressure	Po_∞	1.2 MPa
Slow widths	w	0.5mm, 1 mm, 2mm
Stagnation Pressure of jet to free stream	Po_j/Po_∞	0, 0.076, 0.15, 0.23, 0.31, 0.46

flow fields are visualized by the Schlieren imaging method and surface pressure distributions are measured in the whole interaction region. The set of experiments were performed with and without aerodynamic fences and it was observed that the fences had a significant impact in maintaining the two dimensionality of the flow, thus improving the data set for validation with the numerical simulations. Oil flow visualisation technique was also used for comparison. Following conclusions were made -

1. With the use of the fences, the location of the upstream separation point moves forward and the peak pressures increase. The effect is more pronounced at higher pressure ratios. A comparison is shown in Figure 2.1.
2. A higher pressure ratio makes the flow features like the bow shock, Mach disk and barrel shock larger, but geometrically similar. It also leads to an increase in upstream separation length and penetration height, but this increase is damped at higher pressure ratios.
3. A wider slot has a similar effect, but it also changes the geometry of the features. The emerging jet looked like a budding type with smaller slot widths and became like a fan when a wider slot was used.

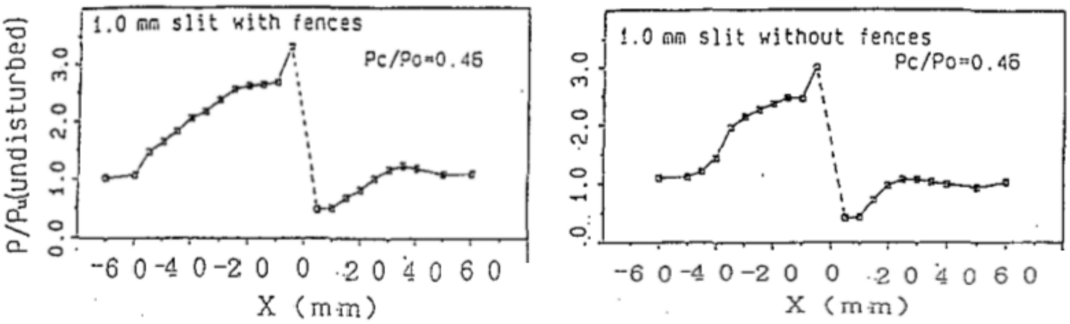

Figure 2.1: Comparison of wall pressure distribution with and without fences in Aso et al.'s experiments[3]

2.1.2 3-D Circular Jet Injection

The work by Morkovin et al.[13] aimed at studying the geometrical and spreading characteristics of the injected jet, along with the inertial forces generated by the injected jet. The free stream Mach was 1.9 and the jet stagnation pressure to free stream static pressure varied from zero to over 50. They used flow visualisation techniques and static wall pressure data for analysis. They concluded that near the body surface, the bending appears to form a low pressure pocket where the mixing is especially violent. Also, for a given nozzle shape, the various lengths characterizing the interaction of the flow field appeared to vary almost linearly with the mass flux in the jet for the range of pressure ratios they investigated.

Spaid and Zukoski[11,12] conducted systematic wind tunnel experiments over a range of freestream Mach numbers of 1.38 to 4.54. The injectants used were gaseous nitrogen, argon, and helium. Pressure fields, concentration fields, and shock shape data was obtained. They suggested that jet penetration height can be used as a scaling parameter for the geometry of the flow field.

Schetz et al.[15] conducted Mach 2.1 (freestream) tests with a flat-plate model. Air was injected through a 3.9 mm diameter sonic nozzle which was placed 50mm from the leading edge at the centre of the 127mm span plate. Tests were run between 758.4kPa down to 117.2 kPa; and the flow field was studied using shadowgraph and schlieren images. They studied the geometrical characteristics of the jet and tried to analytically correlate them with previous theoretical results and data available of jet injection into a quiescent medium, using a parameter -

'effective back pressure (P_{eb})'. The concept of effective back pressure can be understood as follows - upstream of the jet, there is a high pressure region due to the bow shock formation whereas downstream there is low pressure. An intermediate pressure can be found which can be used for comparison with cases of injection into a quiescent medium. The correlation was best achieved using 0.8 of the static pressure behind a normal shock in the freestream as the effective back pressure. They used data from other experiments too, and the total data for Mach numbers ranged from 1.9-4.5, and the P_j/P_{eb} from 1 to 60. Further, they observed that the horizontal displacement of the center of the Mach disc was almost equal to its vertical height from the injector. A previous study[14] also showed that the momentum flux ratio J (or dynamic pressure ratio) given by,

$$J = \rho_j u_j^2 / \rho_\infty u_\infty^2 \tag{2.1}$$

is an important parameter to study the flow fields. Several results[16, 14] indicate that the jet's penetration into the supersonic crossflow is principally dependent on the momentum flux ratio defined in Equation 2.1. There is little or no effect due to the freestream or jet Mach numbers.

For cases with a high initial J, underexpansion was shown to be detrimental to the penetration of a given amount of injected fluid. For J = 1, underexpansion seemed slightly beneficial. Schetz and Billig[14] suggested that injection at a pressure-matched condition (i.e., where the static pressure of the jet is equal to the effective back pressure) produced a more optimum penetration than simply over-pressurizing the jet, due to reduced shock losses.

Aso et al.[3] also conducted 3D experiments with the setup and flow conditions similar to the 2D case shown in Table 2.1. The difference is that instead of a slot injection, circular holes of 3mm and 5mm were used. The ratios of total pressure of jet to freestream were 0.15, 0.31 and 0.46. Apart from wall static pressure measurements, data of oil flow visualisations is also available. One of which is shown in Figure 2.2. These visualisations suggest the presence of a horse shoe vortex curving around the jet as expected.

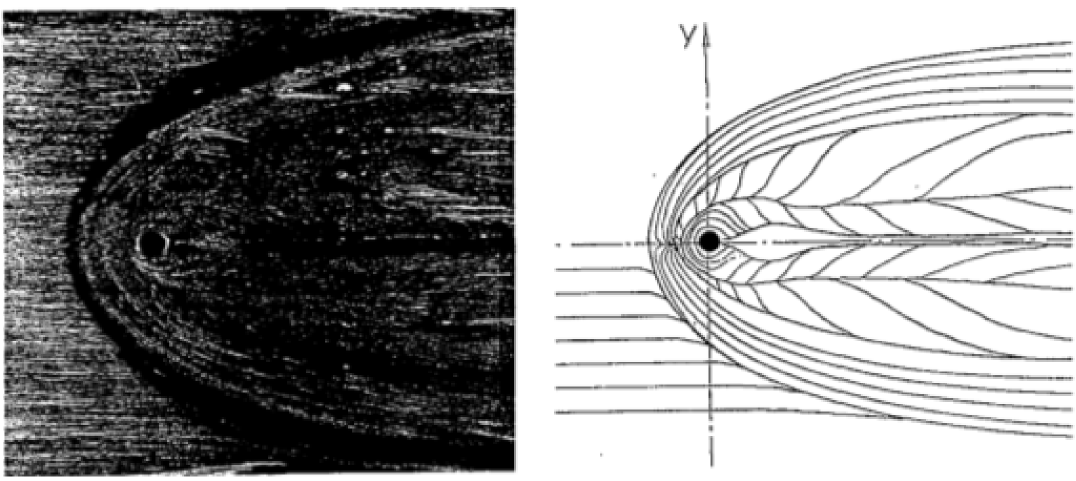

Figure 2.2: Aso's oil flow visualisations for a total pressure ratio of 0.31[3]

A study of previous data by Grubber et al.[16] compares the flow fields for different shapes (circular, elliptical) and inclinations (transverse, oblique) of the injector orifice. The injector exit geometry does not affect the transverse penetration of the jet in the near field, but there is considerable variation in the lateral mixing for elliptical jets when compared to circular. The elliptical injection with the major axis aligned with the freestream flow resulted in a smaller separation zone and standoff distance and a weaker bow shock compared with circular injection. The injector orientation determines the obstruction to the freestream, and consequently the pressure loss due to the strength of the bow shock. Although high oblique angles lead to faster mixing in the near field, not much mixing advantage was found in the far field regions.

Santiago and Dutton[17] conducted tests in a freestream of Mach 1.6 where the underexpanded sonic jet is injected through a 4mm nozzle. Apart from the classic Schlieren and shadowgraph flow visualisations, this study also provides data from Laser Doppler Velocimetry measurements which helps us measure three mean velocity components, five of the six kinematic Reynolds stresses, and turbulent kinetic energy at over 4000 locations throughout the flow field. Everett et al.[18] performed experiments with some conditions similar to that of Santiago et al. using Pressure Sensitive Paint (PSP) to determine the continuous surface pressure field.

Another experimental study recently conducted as a part of a PhD thesis at IISc[19] studies the flowfield and mixing associated with transverse jet injection through a circular and square hole at J=1.5,2,2.5 and 3. An important take away from the work is the high corelation between the separation shock location and boundary layer velocity fluctuation. The enhancement of mixing using a novel passive modulated jet is also explored by them.

2.2 Simulations

2.2.1 2-D Slot Injection

A brief overview of the simulations performed for Aso et al.'s slot injection experiment is given here.[4] In 1962, Rizzetta[20] used an explicit MacCormack scheme and k-ϵ equations. By using an explicit compressibility modeling, significant improvements were seen in the matching of upstream pressure rise and peak pressure region with experimental data. However, the reference data[2] itself had shortcomings due to three dimensionality effects because of the absence of aerodynamic fences. Also, there were a limited number of pressure tabs, and hence the experimental data was highly discontinuous. The scheme had no inclusion of the turbulent kinetic energy in the total energy term, and hence there would be considerable error with this data.

Gerlinger et al.[22] used a q - ω (where q = $\sqrt{k}$) turbulence model because previous k-ω simulations had not been stable. Transport equations for q and ω were decoupled from the other transport equations for stability. Three types of corrections to the standard turbulence model were assessed. One is a limit on ω, the second is assigning a different value of a model constant in the ω-equation, and the third is the compressibility correction (same as that used in Rizzeta's model). The effect of the first two modifications applied together was found to be approximately the same as that due to the third alone. Only the first two modifications were retained. A central differencing scheme with matrix artificial dissipation was used. Velocity magnitude scaling was done to keep dissipation low.

The injector region has several flow structures such as shocks, separated flows and shear layer-shock interactions which cause Reynolds stresses to develop in different ways. Since two equation eddy viscosity models cannot take this anisotropy into consideration, Chenault and Beran[21] examined whether improvements can be realized by using Reynolds stress transport models (RSTM). A Roe scheme with MUSCL (Monotone Upwind Scalar Conservation Law) was used, and there was no explicit compressibility modelling included. Like Gerlinger, they too used the old results of Aso et al.[2] which has several drawbacks. The authors reflected that a better turbulence model is necessary and external factors such as difference of boundary conditions in simulations vs experiments is to be blamed for the disparity in results at high injection pressure ratios.

In all the previous simulations it was seen that at higher pressure ratios, the errors in prediction increased. An example is shown in Figure 2.3. The upstream separation length was usually under predicted and the peak pressures were higher in the simulations as compared to the experiment. The disparity increased with slot width.

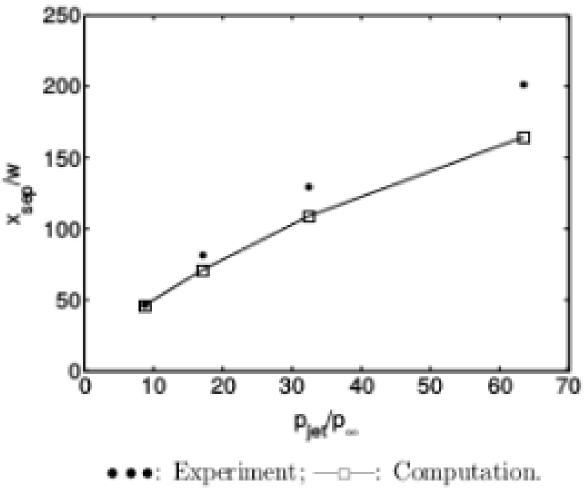

Figure 2.3: Increase in the error of simulations at higher pressures as studied by Mathew and Sriram[4]

Mathew and Sriram[4] attempted to improve the results at high pressure ratios by including low Reynolds number corrections and increasing the grid resolution. The necessity of the former point was explained due to the presence of recirculation zones which are typically having a low Reynolds number. The grid resolution was done not only at the boundary layer, but also uptil the Mach disc, since that region eventually affects the upstream separation. They used a k-w model with explicit compressibility corrections as suggested by Wilcox. At high pressure ratios, inclusion of this correction had stabilising effects. The inviscid fluxes were calculated by the Roe scheme, and a MUSCL scheme was used for extrapolating variables to get a higher order accuracy. The Favre averaged Navier Stokes Equations were integrated to steady states using a six stage, low storage Runge Kutta method. Good results were achieved, even at large pressure ratios, leading to the conclusion that a simple two equation turbulence model, when given corrections for compressibility and low Reynold's number, and a proper grid resolution at the boundary layer and the Mach disc, will give a reasonably good solution. Figure 2.4 shows the comparison of the k-w results of Mathew and Sriram with the previous simulations. They are close to RSTM solution, although the pressure peak is absent in the RSTM results.

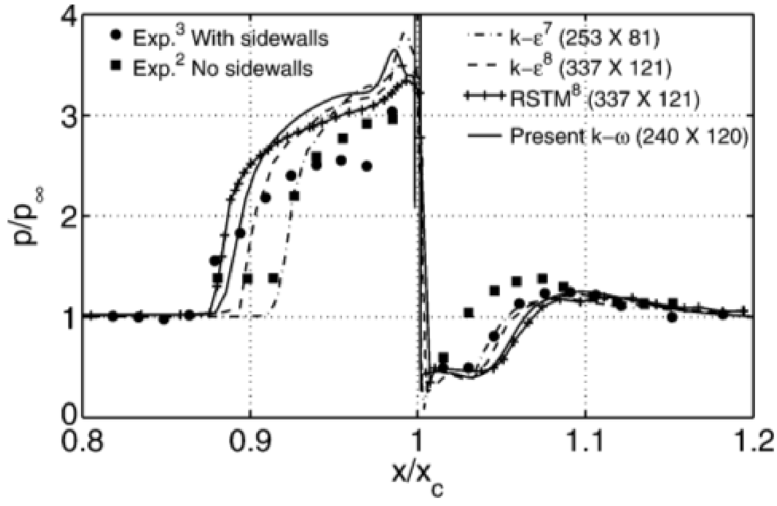

Figure 2.4: Comparison of k-w solution of Mathew and Sriram with previous data[5]

2.2.2 3-D Circular Jet Injection

Mathew and Sriram[6] simulated the 3D injection experiments of Santiago and Dutton,[17] as well as Aso et al.[3] They used a k-ω model, along with compressibility corrections proposed by Wilcox. The governing equations were cast into a standard finite volume formulation. The vector U was the average over the cell and numerical fluxes at cell interfaces were calculated using Roe's approximation to the Riemann solution. The viscous parts of the fluxes were obtained by evaluating derivatives to second order. A semi-implicit version of the Runge-Kutta method was used for fast convergence. They compared different order schemes, because higher-order schemes are more important in three-dimensional simulations where grid refinement alone can become expensive. Residues fell through several decades when either the first-order scheme, or the second-order scheme with minimum modulo (minmod) limiter were used. With the third-order scheme and Van Albada limiter, the fall is less (about four decades)(see Figure 2.5a). However, the solution in Figure 2.5b shows that this lesser fall is still adequate. The second order scheme is sufficient for getting the converged result.

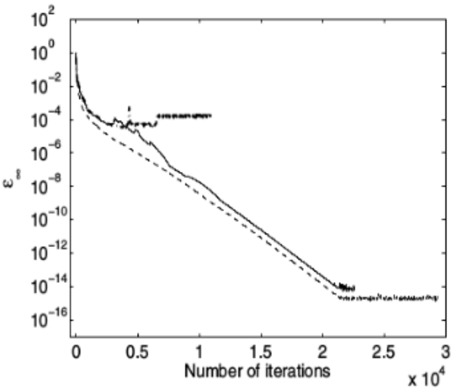

Scaled residue history in L^∞ of ρ for schemes of different orders on the medium grid. Dashed line: first-order; solid line: second-order MUSCL with minmod limiter; dash-dotted line: third-order MUSCL with Van Albada limiter.

(a) Residual plot

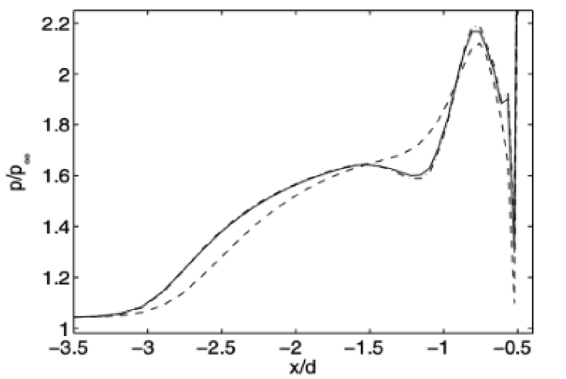

Comparison of wall pressure distribution on 120 × 60 × 60 grid. Dashed line: first-order scheme, solid line: second-order scheme, dash-dotted line: third-order scheme.

(b) Wall pressure along the symmetry axis

Figure 2.5: Results of different order schemes for 3D simulations[6]

The grid of 120 x 60 x 60 cells was found to be adequate. A comparison of the Mach contour for the Santiago and Dutton experiment show that the salient features have been captured by the simulations. The diffuse structures of the measured values may be accounted to unsteadiness. The simulations show a higher jet expansion and

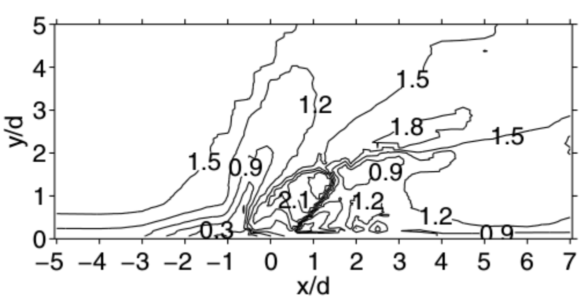

(a) LDV measurements of Santiago and Dutton

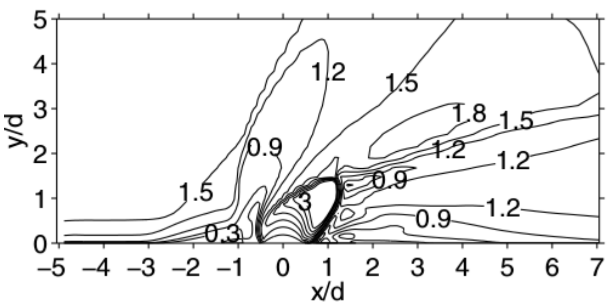

(b) Simulation results of Mathew and Sriram[6]

Figure 2.6: Comparison of Mach contours[6]

consequently a stronger Mach disc shock. The pressure contours give an underprediction of separation length as also seen in 2D simulations. Comparison of mean turbulence quantities, and oil-flow and shear stress contours was also done by the group.[6]

2.3 Summary

Although some experiments have been conducted in the past for JICF at supersonic speeds, the high energy demands and sensitive nature of the flow makes its imperative that we have reliable simulation models to predict the flow. The review of literature showed us that standard two equation models are insufficient and we either require to modify them with certain corrections and use higher order schemes; or use more complex, advanced models such as the Reynolds Stress Transport Model. This led us to the formulation of our Project's Objective.

2.3.1 Project Objective

1. Validating the in-house code (k-ω model) for an experimental case of jet in supersonic cross-flow. The data of Aso et al.[3] is taken as reference.
2. Instead of applying the commonly used compressibility correction, which often distorts the boundary layer; we attempt to capture the true flow physics by implementing a Shock Unsteadiness modification (the details of which are elaborated in Chapter 4).
3. Evaluate the improvement in k-ω model after modifying it with the SU correction.
4. Since wall pressure distribution plots are most readily available in literature, we will be using that data for comparison. Further, we will calculate the disparity in the upstream separation length to quantify the errors arising from different models.

Chapter 3

Simulation Methodology

3.1 Governing Equations

The flow is governed by principles of mass conservation, momentum conservation and energy conservation. These physical laws come together in a set of equations -

$$\frac{\partial \rho}{\partial t} + \frac{\partial (\rho u_i)}{\partial x_i} = 0 \tag{3.1}$$

$$\frac{\partial (\rho u_i)}{\partial t} + \frac{\partial (\rho u_i u_j)}{\partial x_j} = -\frac{\partial p}{\partial x_i} + \frac{\partial \tau_{ij}}{\partial x_j} + \rho f_i \tag{3.2}$$

$$\frac{\partial (\rho e)}{\partial t} + \frac{\partial (\rho e + p) u_i}{\partial x_i} = \frac{\partial (\tau_{ij} u_j)}{\partial x_i} + \rho f_i u_i + \frac{\partial (\dot{q}_i)}{\partial x_i} + s \tag{3.3}$$

Where,

t = Time $\quad$ x_i = Length in i^{th} direction

ρ = Density $\quad$ u_i = Velocity in i^{th} direction

p = Pressure $\quad$ $\dot{q}_i$ = Heat flux

e = Internal energy per unit mass

s = Energy source term

τ_{ij} = Element of stress tensor obtained by Stoke's hypothesis

f_i = Additional body forces per unit mass

Equations 3.1 , 3.2 and 3.3 represent the mass, momentum and energy conservation respectively for an infinitesimal control volume. They are the Navier Stokes (N-S) Equations written in the conservative form.

The Reynold's Average Navier Stokes Equations For turbulent flows, N-S equations are difficult to solve exactly, and hence we use a system of time averaged equations which are the Reynold's Average Navier Stokes equations. Further, the 3D conservation form of the system of equations can be written as -

$$\frac{\partial U}{\partial t} + \nabla . \left(\vec{F} + \vec{G} + \vec{H} \right) = Q, \tag{3.4}$$

where U is the set of conservative variables, $\vec{F}$ is the flux vector in streamwise direction, $\vec{G}$ is the flux vector in flow normal direction, $\vec{H}$ is the flux vector in the spanwise direction and Q is the source term. Using a $k-\omega$ model for calculation of the eddy viscosity in the RANs equations, U can be written as,

$$U = \left[\begin{array}{ccccccc} \overline{\rho} & \overline{\rho}\widetilde{u} & \overline{\rho}\widetilde{v} & \overline{\rho}\widetilde{w} & \overline{\rho}\widetilde{E} & \overline{\rho}k & \overline{\rho}\omega \end{array} \right]^T, \tag{3.5}$$

where superscript T stands for the transpose of the matrix. Thus, a total of seven equations are solved simultaneously to obtain seven conservative variables $\overline{\rho}$, $\overline{\rho}\widetilde{u}$, $\overline{\rho}\widetilde{v}$, $\overline{\rho}\widetilde{E}$, $\overline{\rho}k$, $\overline{\rho}\omega$. Here, $\widetilde{E}$ is the total mean flow energy. The conservative variables are made up of the primitive variables - mean streamwise, wall normal and spanwise velocities $\widetilde{u}$, $\widetilde{v}$ and $\widetilde{w}$ respectively, mean density $\overline{\rho}$, temperature $\widetilde{T}$, total kinetic energy k and the dissipation of turbulent kinetic energy ω. The mean pressure $\overline{p}$ is obtained from perfect gas equation. Solution is obtained for one continuity, three momentum, one energy, one turbulent kinetic energy, and one dissipation of turbulent kinetic energy equations.

The total fluxes are split into inviscid and viscous part. The subscripts I and V represent the inviscid and viscous terms. These equations are written in Cartesian form as[7] ,

$$\frac{\partial U}{\partial t} + \nabla.\left(\vec{F} + \vec{G} + \vec{H}\right) = Q, \tag{3.6}$$

where,

$$F = F_I - F_V; \qquad G = G_I - G_V; \qquad H = H_I - H_V; \tag{3.7}$$

$$F_I = \begin{bmatrix} \overline{\rho}\widetilde{u} \\ \overline{\rho}\widetilde{u}^2 + \overline{p} + \frac{2}{3}\overline{\rho}k \\ \overline{\rho}\widetilde{u}\widetilde{v} \\ \overline{\rho}\widetilde{u}\widetilde{w} \\ \left(\overline{\rho}\widetilde{E} + \overline{p} + \frac{2}{3}\overline{\rho}k\right)\widetilde{u} \\ \overline{\rho}\widetilde{u}k \\ \overline{\rho}\widetilde{u}\omega \end{bmatrix}; \quad G_I = \begin{bmatrix} \overline{\rho}\widetilde{v} \\ \overline{\rho}\widetilde{u}\widetilde{v} \\ \overline{\rho}\widetilde{v}^2 + \overline{p} + \frac{2}{3}\overline{\rho}k \\ \overline{\rho}\widetilde{w}\widetilde{v} \\ \left(\overline{\rho}\widetilde{E} + \overline{p} + \frac{2}{3}\overline{\rho}k\right)\widetilde{v} \\ \overline{\rho}\widetilde{v}k \\ \overline{\rho}\widetilde{v}\omega \end{bmatrix} \quad H_I = \begin{bmatrix} \overline{\rho}\widetilde{w} \\ \overline{\rho}\widetilde{u}\widetilde{w} \\ \overline{\rho}\widetilde{v}\widetilde{w} \\ \overline{\rho}\widetilde{w}^2 + \overline{p} + \frac{2}{3}\overline{\rho}k \\ \left(\overline{\rho}\widetilde{E} + \overline{p} + \frac{2}{3}\overline{\rho}k\right)\widetilde{w} \\ \overline{\rho}\widetilde{w}k \\ \overline{\rho}\widetilde{w}\omega \end{bmatrix} \tag{3.8}$$

$$F_V = \begin{bmatrix} 0 \\ \overline{t_{xx}} + \tau_{xx} \\ \overline{t_{yx}} + \tau_{yx} \\ \overline{t_{yz}} + \tau_{zx} \\ \left(\overline{t_{xx}} + \tau_{xx}\right)\widetilde{u} + \left(\overline{t_{yx}} + \tau_{yx}\right)\widetilde{v} + \left(\overline{t_{zx}} + \tau_{zx}\right)\widetilde{w} + (\kappa + \kappa_T)\,\frac{\partial \widetilde{T}}{\partial x} + \left(\mu + \frac{\mu_T}{\sigma_k}\right)\frac{\partial k}{\partial x} \\ \left(\mu + \frac{\mu_T}{\sigma_k}\right)\frac{\partial k}{\partial x} \\ \left(\mu + \frac{\mu_T}{\sigma_k}\right)\frac{\partial \omega}{\partial x} \end{bmatrix} \tag{3.9}$$

$$G_V = \begin{bmatrix} 0 \\ \overline{t_{xy}} + \tau_{xy} \\ \overline{t_{yy}} + \tau_{yy} \\ \overline{t_{zy}} + \tau_{zy} \\ \left(\overline{t_{xy}} + \tau_{xy}\right)\widetilde{u} + \left(\overline{t_{yy}} + \tau_{yy}\right)\widetilde{v} + \left(\overline{t_{zy}} + \tau_{zy}\right)\widetilde{w} + (\kappa + \kappa_T)\,\frac{\partial \widetilde{T}}{\partial y} + \left(\mu + \frac{\mu_T}{\sigma_k}\right)\frac{\partial k}{\partial y} \\ \left(\mu + \frac{\mu_T}{\sigma_k}\right)\frac{\partial k}{\partial y} \\ \left(\mu + \frac{\mu_T}{\sigma_k}\right)\frac{\partial \omega}{\partial y} \end{bmatrix} \tag{3.10}$$

$$H_V = \begin{bmatrix} 0 \\ \overline{t_{xz}} + \tau_{xz} \\ \overline{t_{yz}} + \tau_{yz} \\ \overline{t_{zz}} + \tau_{zz} \\ \left(\overline{t_{xz}} + \tau_{xz}\right)\widetilde{u} + \left(\overline{t_{yz}} + \tau_{yz}\right)\widetilde{v} + \left(\overline{t_{zz}} + \tau_{zz}\right)\widetilde{w} + (\kappa + \kappa_T)\,\frac{\partial \widetilde{T}}{\partial z} + \left(\mu + \frac{\mu_T}{\sigma_k}\right)\frac{\partial k}{\partial z} \\ \left(\mu + \frac{\mu_T}{\sigma_k}\right)\frac{\partial k}{\partial z} \\ \left(\mu + \frac{\mu_T}{\sigma_k}\right)\frac{\partial \omega}{\partial z} \end{bmatrix} \tag{3.11}$$

$$Q = \begin{bmatrix} 0 & 0 & 0 & 0 & 0 & (P_k - \beta^*\overline{\rho}k\omega) & \left(\alpha\frac{\omega}{k}P_k - \beta\overline{\rho}\omega^2\right) \end{bmatrix}^T \tag{3.12}$$

$\overline{t_{xx}}$, $\overline{t_{xy}}$, $\overline{t_{yy}}$ are the mean viscous stresses acting on fluid particles, τ_{xx}, τ_{xy}, τ_{yy} are the Reynolds stresses and P_k represents the production term of the turbulent kinetic energy. μ represents the viscosity of the fluid, with μ_T refering to the eddy viscosity. Mathematically, $\mu_T = \rho k/\omega$. Similarly, κ and κ_T stand for the conductivity and turbulent conductivity.

3.2 Numerical Methods

The exact analytical solutions of these partial differential equations are difficult to obtain. We discretize them into a system of algebraic equation. Generally, the Taylor series expansion is used to approximate the equations to system of algebraic linear equations. There are several discretisation methods such as finite difference (FDM), finite element (FEM) and finite volume (FVM). We are using the FVM approach.

3.2.1 Finite Volume Formulation

Finite Volume Formulation of the above system is done as follows.[7] The system is reduced to a two-dimensional system for the sake of simplicity of explanation. The conservation equation 3.4 is integrated over the control surface area (CS) of control volume (CV) to give:

$$\frac{\partial}{\partial t}\iiint_{CV} U\, dV + \iint_{CS}\left[\left(\vec{F_I}+\vec{G_I}\right)+\left(\vec{F_V}+\vec{G_V}\right)\right].(\hat{n}dS) = Q \tag{3.13}$$

Here $\hat{n}$ is unit normal vector to surface area dS as shown in Figure 3.1. For an infinitesimal volume -

$$\frac{\partial U}{\partial t} = -\frac{1}{V_{i,j}}\left[\vec{F}_{i+1/2,j}.\vec{S}_{i+1/2,j}+\vec{F}_{i-1/2,j}.\vec{S}_{i-1/2,j}+\vec{G}_{i,j+1/2}.\vec{S}_{i,j+1/2}+\vec{G}_{i,j-1/2}.\vec{S}_{i,j-1/2}\right]+Q, \tag{3.14}$$

$$\begin{aligned}\vec{S}_{i+1/2,j} &= \left(y_{i+1,j+1}-y_{i+1,j}\right)\hat{\imath}-\left(x_{i+1,j+1}-x_{i+1,j}\right)\hat{\jmath}\\ \vec{S}_{i-1/2,j} &= -\left(y_{i,j+1}-y_{i,j}\right)\hat{\imath}+\left(x_{i,j+1}-x_{i,j}\right)\hat{\jmath},\end{aligned} \tag{3.15}$$

$$\begin{aligned}V_{i,j} = [|&\left(x_{i,j}-x_{i+1,j}\right)y_{i+1,j+1}+\left(x_{i+1,j}-x_{i+1,j+1}\right)y_{i,j}+\left(x_{i+1,j}-x_{i,j}\right)y_{i+1,j}|\\ +|&\left(x_{i,j}-x_{i+1,j+1}\right)y_{i,j+1}+\left(x_{i+1,j+1}-x_{i,j+1}\right)y_{i,j}+\left(x_{i,j+1}-x_{i,j}\right)y_{i+1,j+1}|]\end{aligned} \tag{3.16}$$

$\vec{S}_{i+1/2,j}$, $\vec{S}_{i-1/2,j}$ are the surface area vectors and $\hat{\imath}$, $\hat{\jmath}$ are unit vectors in i and j direction.x and y are the coordinates of the grid points and $V_{i,j}$ is the control volume. The calculation of $\vec{S}_{i,j-1/2}$ is explained in Figure 3.1.

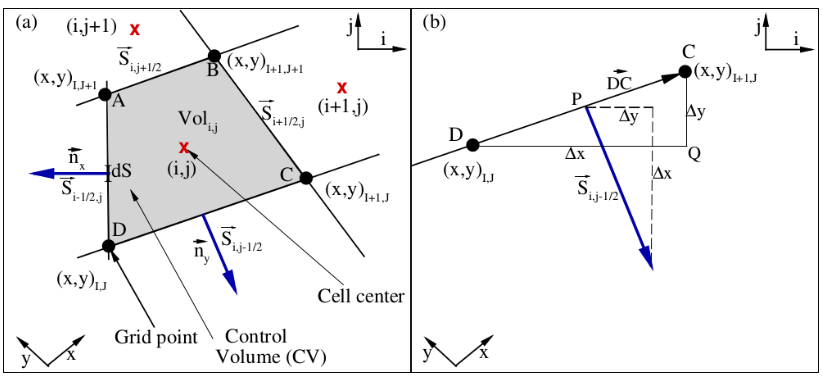

Figure 3.1: (a) Two-dimensional control volume used in finite volume formulation, where the grid points are represented by black solid circles with capital indices of I and J and cell centers are shown by crosses represented by small indices of i and j and (b) Calculation of normal surface vector $\vec{S}_{i,j-1/2}$.[7]

3.2.2 Elliptic and Hyperbolic Equations

As we saw in Chapter 1, the high speed crossflow interaction has complex features and all of these need to be captured accurately using appropriate CFD techniques. For the steady-state solution of high speed flows the hyperbolic and elliptic nature of the equations influence the numerics.

The diffusive terms dominate in boundary-layer and separated flows. In such subsonic recirculation regions, the information can flow in all the directions and the flow possesses elliptic nature. The **central differencing scheme** can be used to discretize the **viscous terms**. The viscous fluxes and the turbulent source terms are calculated using second-order accurate central difference method.

The convective terms dominate in the **inviscid regions** and the flow is hyperbolic in nature and in space. The inviscid fluxes are solved using the **Steger-Warming flux splitting method**.[8] The implicit Data Parallel Line Relaxation (DPLR) method of Wright et al.[9] is used to integrate the equations in time to reach a steady-state solution.

3.2.3 Steger Warming Method

The Steger-Warming[8] method is used for high speed inviscid flows to capture shock waves by taking the advantage of the hyperbolic nature of the Euler equations. The basic requirement for hyperbolic flow is that the eigen values should be real, distinct and positive. The upwind discretization method is used to solve the governing equations. In an upwind scheme spatial differencing is done on the mesh points on the side from which the information or wind flows. Upwind schemes use information of the local wave propagation explicitly. The eigen values provide the direction of information in the flow. In one dimension, the flux vector is function of the conservative variable vector and is evaluated as,

$$[F] = [A]\,[U] \tag{3.17}$$

where A is the Jacobian matrix and U is the conserved variables vector. The Jacobian matrix, A is calculated by taking the partial derivative of the flux-vector with respect to the vector of conserved variables.

$$A = \begin{bmatrix} \frac{\partial F_1}{\partial U_1} & \frac{\partial F_1}{\partial U_2} & \frac{\partial F_1}{\partial U_3} \\ \frac{\partial F_2}{\partial U_1} & \frac{\partial F_2}{\partial U_2} & \frac{\partial F_2}{\partial U_3} \\ \frac{\partial F_3}{\partial U_1} & \frac{\partial F_3}{\partial U_2} & \frac{\partial F_3}{\partial U_3} \end{bmatrix} \tag{3.18}$$

$$= \begin{bmatrix} 0 & 1 & 0 \\ (\gamma-3)\,u^2/2 & (3-\gamma)\,u & (\gamma-1) \\ (\gamma-1)\,u^3 - \gamma eu/\rho & \gamma e/\rho - 3\,(\gamma-1)\,u^2/2 & \gamma u \end{bmatrix} \tag{3.19}$$

With this Jacobian matrix we write the characteristic equation to find the eigen values.

$$det\,[A - \lambda I] = 0 \tag{3.20}$$

where I is the identity matrix. The three eigen values of the above matrix are

$$\Lambda = \begin{bmatrix} u & 0 & 0 \\ 0 & u+a & 0 \\ 0 & 0 & u-a \end{bmatrix} \tag{3.21}$$

Here u is speed of the flow and a corresponds to the speed of the sound. For each eigen value the corresponding eigen vectors are calculated as,

$$[A]\left[r_i^1 r_i^2 r_i^3\right]^T = \lambda_i \left[r_i^1 r_i^2 r_i^3\right]^T \tag{3.22}$$

Each of the these single column 1×3 matrix of eigen vectors are arranged in three columns of a 3×3 square matrix to form a right eigen vector matrix T as given by Equation 3.23. The corresponding left eigen vector matrix is evaluated as T^-.

$$[T] = \left[|r_k^p||r_k^p||r_k^p|\right] \tag{3.23}$$

Here $p = (1, 2, 3)$ and $k = (1, 2, 3)$. $|r_k^p|$ corresponds to the single column matrix formed by calculating the eigen vector from Equation 3.22 for corresponding eigen value k. Using T and T^- the negative and positive Jacobian matrices are calculated. The Jacobian is split into positive and negative parts by splitting the eigen values into positive and negative parts. The diagonal matrix Λ_+ contains only positive eigen values and diagonal matrix Λ_- has only negative eigen values.

$$A = A_+ + A_- \tag{3.24}$$

$$\lambda_k = \lambda_{k+} + \lambda_{k-} \tag{3.25}$$

$$\lambda_{k+} = \frac{\lambda_k + |\lambda_k|}{2} \tag{3.26}$$

$$\lambda_{k-} = \frac{\lambda_k - |\lambda_k|}{2} \tag{3.27}$$

$$\Lambda = \Lambda_+ + \Lambda_- \tag{3.28}$$

$$\Lambda_+ = diag\left(\frac{\lambda_k + |\lambda_k|}{2}, \frac{\lambda_k + |\lambda_k|}{2}, \frac{\lambda_k + |\lambda_k|}{2}\right) \tag{3.29}$$

$$\Lambda_- = diag\left(\frac{\lambda_k - |\lambda_k|}{2}, \frac{\lambda_k - |\lambda_k|}{2}, \frac{\lambda_k - |\lambda_k|}{2}\right) \tag{3.30}$$

$$A_+ = T\Lambda_+ T^-; \qquad A_- = T\Lambda_- T^- \tag{3.31}$$

The fluxes are then split according to the sign of the Jacobians as positive and negative parts as below.

$$F = F_+ + F_- \tag{3.32}$$

$$F_+ = A_+ U; \qquad F_- = A_- U \tag{3.33}$$

The explicit time integration is carried out by

$$U_i^{n+1} = U_i^n - \frac{\Delta t}{\Delta x}\left[(F_{+_i} + F_{-i+1}) - (F_{+_{i-1}} + F_{-i})\right]^n, \tag{3.34}$$

where n is the current time step and n+1 is the next time step. In a control volume these fluxes are calculated at the cell faces with the help of the Jacobian and the values of conservative variables are taken from the cell center.

3.3 Comparison of Turbulence Models

There are several models developed for studying turbulent flows. The simplest one is a one equation Spallart Allmaras model. Then we have two equation models such as the standard $k - \omega$ and $k - \epsilon$ models. These take in an eddy viscosity hypothesis. The use and significance of some of the models is briefly understood here.

The Spallart Allmaras Model

- 1 equation model, solves a transport equation for a viscosity like variable $\widetilde{\nu}$
- Developed and used for wall-bounded, aerodynamic flows. Not a good model for modelling round jet flows.
- It gives good results for boundary layer flows even with large pressure gradients

The k - ϵ model

- 2 equation model, solves for the turbulent kinetic energy - k and the rate of dissipation (ϵ) of k
- Good for predicting flow variables far from walls, plane shear layers and recirculating flows.
- It does not give good results for flows with large pressure gradients. It should not be used for unconfined/rotating flows/curved boundary layer flows.

The k - ω model

- 2 equation model, solves for the turbulent kinetic energy - k and the specific rate of dissipation (ω) of k into thermal energy.
- Good for near wall predictions.
- Solves for turbulent eddy viscosity - $\mu_T = \rho k/\omega$. The total viscosity is then $\mu_{total} = \mu + \mu_T$

Shear Stress Transport (SST) Model

- Combines the k - ω and k - ϵ model for good results near as well as far from wall

Reynold's Stress Transport Model (RSTM)

- The most complete model.
- It has no hypothesis of the eddy viscosity, but in fact, calculates every component of the Reynold's Stress Tensor.

3.4 Summary

We listed the Reynolds Average Navier Stokes Equations for the standard k-ω model, along with the concept of finite volume formulation. The hyperbolic nature of supersonic flows engenders the need for a flux splitting numerical method - the Steger Warming Scheme, which has been explained here in detail. Our simulations are run on the k-ω model, but the applications and uses of various other turbulence models are also briefly discussed.

Chapter 4

The Shock Unsteadiness Model

4.1 Drawbacks of Standard Model

Standard RANS turbulence models, like k-ϵ and k-ω, cannot accurately predict flows with strong shocks and their interaction with turbulence. Disagreement with experimental data is seen for problems such as compression corner flows and oblique shock impingement on boundary layer. The inconsistency is greater at large Mach numbers and higher ramp angles. The standard models are unable to satisfactorily predict the size of the separation region, peak heat transfer rates at re-attachment etc. This drawback is also seen in our present problem. Standard k-w model highly under-predicts the upstream separation length and peak pressures.

Sinha et al.[1] point out that such variations from experimental results are due to the over-amplification of turbulent kinetic energy (k) across the shock wave by standard models. The over estimation of k leads to a more energized boundary layer, which is able to sustain the adverse pressure gradient created by the shock waves for longer, thus delaying flow separation. The over-amplification of k is partly due to the fact that the standard models do not consider the unsteady nature of shock wave while interacting with turbulence. Upstream turbulence makes the shock oscillate about a mean position and the amplification of turbulence across an unsteady shock is less compared to its amplification across a steady shock wave.

Several other modifications to standard model - e.g., realizability constraint, compressibility correction, length-scale modification and rapid compression correction have been suggested. However, the outcome of these modifications vary from model to model and also with the test conditions, which point to the possibility that some key physical processes are either modelled incorrectly or not included in the model.[1]

Sinha et al.[1] modelled the unsteady effect of shock waves in the otherwise steady RANS framework and incorporated the unsteady shock physics into standard turbulence models. The shock-unsteadiness modified turbulence models are found to improve the flow topology significantly, thereby giving better predictions for surface pressure and separation bubble size, in flows with shock-shock and shock-boundary layer interactions.[24,25,26]

4.2 Mathematical Formulation of SU Model

In the standard k-ω model, the production term in turbulent kinetic energy equation is given as follows -

$$P_k = \mu_T \left(2S_{ij}S_{ji} - \frac{2}{3}S_{ii}^2 \right) - \frac{2}{3}\overline{\rho}kS_{ii} \tag{4.1}$$

where $S_{ij} = \frac{1}{2}\left(\partial\widetilde{u_i}/\partial x_j + \partial\widetilde{u_j}/\partial x_i\right)$ and $\widetilde{u_i}$ is the component of the Favre-averaged velocity in the i-direction. Here, the over-bar and tilde represent the Reynolds and Favre-averaged quantities respectively and the turbulent eddy viscosity is modelled as $\mu_T = \overline{\rho}k/\omega$.

Sinha et al.[1] state that in a highly non-equilibrium flow such as shock-turbulence interaction, the concept of eddy viscosity breaks down and the usual model with μ_T gives unrealistically high values of Reynolds Stresses, which in turn lead to a large production term and over-prediction of the turbulent kinetic energy. To overcome this, one may suppress μ_T to zero, which gives -

$$P_k = -\frac{2}{3}\overline{\rho}kS_{ii} \tag{4.2}$$

However, keeping $\mu_T = 0$ reduced this over-prediction only at lower shock Mach numbers (<1.5). See Figure 4.1. The error was still large at higher Mach values. This indicated that completely suppressing μ_T is a limiting case and is alone not sufficient for accurate prediction of k.

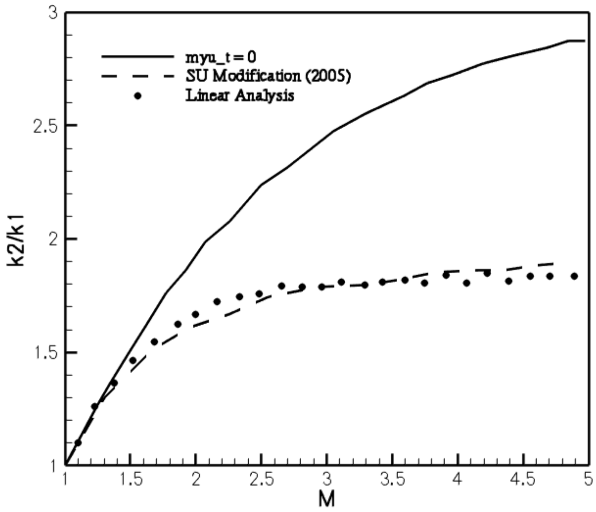

Figure 4.1: Impact of SU modification on turbulent kinetic energy k[1]

Consequently, Sinha et al.[1] modelled the shock as having a distortion with velocity ξ_t in the shock normal direction and angular distortions ξ_y and ξ_z in the shock plane. It was seen that the shock unsteadiness due to ξ_t damped the production of u'^2 , (u'^2 being the turbulent velocity fluctuation in the shock normal direction) whereas the angular shock distortions ξ_y and ξ_z amplified the production of v'^2 and w'^2 respectively. This led to the introduction of a model coefficient b' such that -

$$P'_k = -\frac{2}{3}\bar{\rho}kS_{ii}\left(1 - b'_1\right), \tag{4.3}$$

Where b' represents the damping effect of unsteady shock oscillations; and was prescribed using Linear Interaction Analysis (LIA) results for canonical shock-turbulence interaction as -

$$b'_1 = \max.[0, 0.4\left(1 - e^{1-M_{1n}}\right)] \tag{4.4}$$

The $max()$ condition was set to ensure that the shock-unsteadiness modification is not applied when $M_{1n} < 1$. As we can see in Figure 4.1, this equation accurately matches the results obtained from linear interaction analysis. It is a better estimate than merely setting $\mu_T = 0$. The shock-unsteadiness damping parameter is a function of the upstream shock-normal Mach number M_{1n}, which brings in the physical effect of the shock strength. It takes a value of 0.4 in the hypersonic limit and vanishes for very weak shock waves. Additional details of the shock-unsteadiness model development are given in references.[1,24,25]

4.3 Implementing SU Modification to k-ω Model

The shock-unsteadiness modification is applied in the k-ω framework by multiplying the production term of the standard k-ω model by the factor,

$$c'_\mu = 1 - f_s\left[1 + \frac{b'_1\omega}{\sqrt{3}S}\right] \tag{4.5}$$

so that,

$$P_k = \left[1 - f_s\left(1 + \frac{b'_1\omega}{\sqrt{3}S}\right)\right] * \mu_T S^2 - \frac{2}{3}\bar{\rho}kS_{ii} \tag{4.6}$$

where,

$$S = \left[2S_{ij}S_{ji} - \frac{2}{3}S_{ii}^2\right]^{1/2} \tag{4.7}$$

and f_s is an empirical shock function to identify regions of high compression, ie, shocks. It smoothly varies between 0 and 1; taking a maximum value of 1 inside shocks. At this condition, Equation 4.6 reduces to Equation 4.3 because the shock normal derivatives in S are much higher than the derivatives in the other directions. Outside shocks, it is zero and the standard form of k-ω model is recovered.

The Shock Function 'f_s' essentially serves as a locator and identifies the region over which the SU modification must be applied and with how much strength. The original form of f_s proposed in 2005 (henceforth addressed as SU 2005) by Sinha et al.[24] for implementation on compression ramp problems was given as -

$$f_s = \frac{1}{2} - \frac{1}{2}tanh\left[5\left(S_{ii}/S\right) + 3\right] \tag{4.8}$$

The impact of this modification on a compression ramp case (ramp angle = 24^o) is shown in Figure 4.2. All plots shown in this chapter are taken from Sinha et al.[1,24] As can be seen, the 2005 modification causes earlier separation as compared to the standard model and predicts the wall pressure distribution along the ramp more correctly.

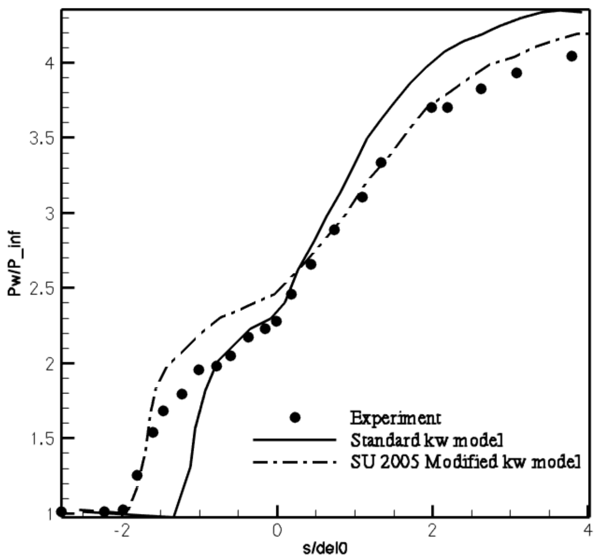

Figure 4.2: Wall pressure ratio results of Sinha et al.[24] for a compression ramp at 24^o

Later, in 2008, while studying the effect of SU modification on problems involving impingement of an oblique shock on a boundary layer, Pasha et al.[25] noticed that the SU 2005 version failed to give satisfactory results due to S taking large values near the boundary layer and incorrectly giving low f_s values. They considered several other ways of normalising S_{ii} and settled on the following form (henceforth addressed as SU 2008) -

$$f_s = \frac{1}{2} - \frac{1}{2}tanh\left[12\left(S_{ii}\delta_0/U_\infty\right) + 4\right] \tag{4.9}$$

Where δ_0 is the characteristic length , taken as the upstream boundary layer thickness; and U_∞ is the freestream velocity. For this thesis, we have presented results using both these versions of the function. Further, the SU 2008 version has also been modified. The coefficients $'12'$ and $'4'$ in the *tanh* function are replaced by variables a and b respectively. The impact of changing these values is then presented in the results.

The Shock Damping Parameter '$b_1^{'}$' represents the impact of the unsteady motion and distortion of the shock wave. As seen in Equation 4.4, it depends on the upstream normal Mach number. For simple problems, this value can be known beforehand. However, for more complex cases involving multiple shocks, the different values of $b_1^{'}$ throughout the domain are difficult to determine *a priori*. Coding it will also be cumbersome. Thus, an average value of the domain can be taken. Alternatively, for our present problem, we have shown results for 4 sets of $b_1^{'}$ values, varying from 0.1 to 0.4. A higher value depicts more impact of shock unsteadiness. The results at $b_1^{'} = 0.4$ can be viewed as a limiting case of the simulation results.

4.4 Summary

The standard k-ω model cannot accurately predict flow phenomenon such as separation bubble size in shock-turbulence interactions due to over-prediction of turbulent kinetic energy post shock. The SU Modification serves to correct this problem by suppressing the turbulent viscosity and incorporating the effects of shock distortions in the production term of k. An important parameter is the shock damping coefficient $b_1^{'}$ that represents the impact of shock unsteadiness. The shock function f_s is a smooth empirical function that helps implement the modification only inside the shock, and reduces the SU modified equation to the standard k-ω form outside the shock.

Chapter 5

Simulation Results

Simulations were performed for two-dimensional transverse injection through a rectangular slot. The flow and geometry conditions matched those of the experiments of Aso et al.[3] The simulations were done using a Steger Warming flux splitting scheme and a standard Wilcox k-w turbulence model as explained in Chapter 3. Consequently, the Shock Unsteadiness modification was implemented. The normalised pressure ratio (NPR) $P_j/P_\infty = 17.7$ is the primary case studied. However, four other NPR cases are also run and compared with the experimental results (shown in Table 5.2). The simulations were run on the implicit Fortran code developed in-house. The postprocessing was done on Tecplot.

5.1 Input Flow Conditions

Table 5.1 summarises the flow properties given as input for NPR 17.7 simulations.

Table 5.1: Flow conditions used for simulations

Freestream Mach	M_∞	3.75	Jet Mach	M_j	1
Freestream Temperature	T_∞	78.43 K	Jet Temperature	T_j	249 K
Freestream Pressure	P_∞	11.09 kPa	Jet Pressure	P_j	196.52 kPa
Freestream Total Temperature	To_∞	299 K	Jet Total Temperature	To_j	298.8 K
Freestream Total Pressure	Po_∞	1.2 MPa	Jet Total Pressure	Po_j	0.372 MPa
Reynolds number	Re	$2 * 10^7$			

The important ratios are calculated as,

$$P_j/P_\infty = 17.72 \tag{5.1}$$

$$Po_j/Po_\infty = 0.31 \tag{5.2}$$

$$J = (\rho u^2)_j/(\rho u^2)_\infty = (\gamma * M_j^2 * P_j)/(\gamma * M_\infty^2 * P_\infty) \tag{5.3}$$

$$= 1.26 \tag{5.4}$$

Table 5.2: Cases of Aso et al.'s experiment simulated with standard $k-\omega$ model[3]

Case	NPR P_j/P_∞	Pressure P_j (kPa)	Density ρ_j (kg/m^3)	J $(\rho u^2)_j/(\rho u^2)_\infty$
1	8.57	95	1.33	0.61
2	13.1	145	2.05	0.93
3	17.7	196	2.76	1.26
4	21.7	240	3.38	1.54
5	25.7	285	4.00	1.83

5.2 Grid Details and Boundary Conditions

The computational domain was divided into three zones - upstream, injector, downstream. The x axis lies along the freestream, the transverse direction is along y, and z axis is in the spanwise direction. Figure 5.1 shows the various zones (note that the leading edge is at x=0 and the domain extends to 0.495m). Table 5.3 lists out the minimum and maximum x values of each zone, along with the cells along each axis (given by X*Y). The y axis extends from 0 to 0.03m for all zones. The domain also spreads in the three dimensional space with z axis length of about 10 mm, and 5 cells along the positive and negative z direction. **Note:** all dimensions are in meters unless mentioned otherwise.

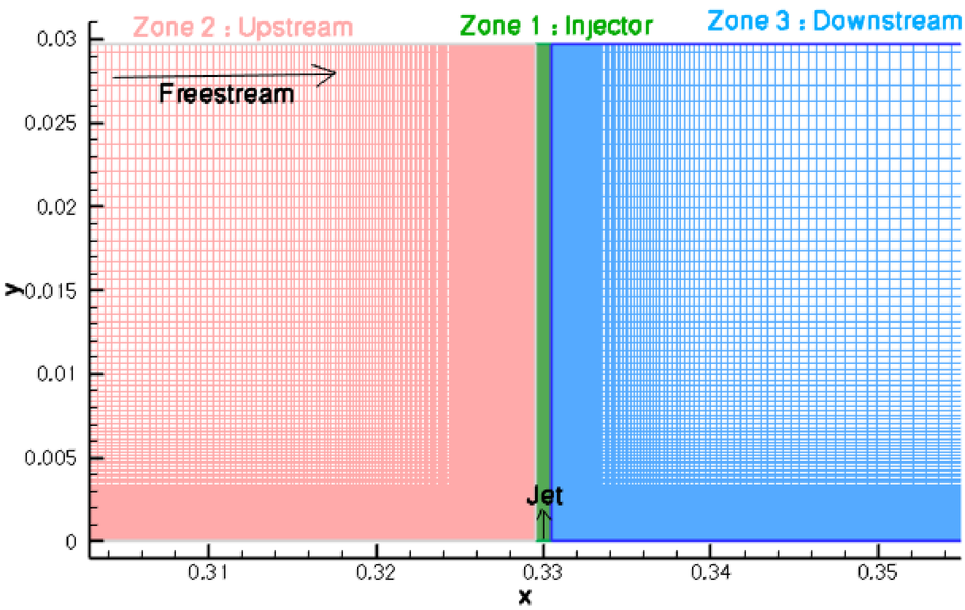

Figure 5.1: Zones of computational domain

Table 5.3: Grid details of individual zones

Zone	x_{min}	x_{max}	Cells	Total cells
1	0.3295	0.3305	25*241	6025
2	0	0.3295	305*241	73505
3	0.3305	0.495	163*241	39283
Entire Domain	0	0.495	493*241	111813

It can be seen from Figure 5.1 that the grid is clustered around the injector location and near the flat plate boundary. Almost **44 % of the cells lie within 10 %** of the height above the plate. The cell height (dy) near the wall is a minimum equaling 2.5E-07 and exponentially increases to 5E-04 at the top boundary. Along the freestream, almost **30 % of the cells are clustered within 5mm** upstream and downstream of the injector. The grid size along x (dx) is minimum of 2.5E-05m near the injector. Upstream it increases upto 0.006m near leading edge and 0.005m downstream at the flow exit boundary. Such a refinement is essential to accurately capture the boundary layer, flow separation zones, mach disc and barrel shock inside the jet boundary.

Boundary conditions are given in Table 5.6. Since we have a three dimensional domain, a periodic boundary condition at the z planes ensures the two dimensionality of the simulated flow. The wall is isothermal at 300K.

Table 5.4: Boundary conditions used in simulations

Zone	xmin	xmax	ymin	ymax	zmin	zmax
1	Interface	Interface	Sonic Jet Inlet	Outflow	Periodic	Periodic
2	Supersonic Inlet	Interface	No slip wall	Outflow	Periodic	Periodic
3	Interface	Outflow	No slip wall	Outflow	Periodic	Periodic

Grid convergence for the given case (standard model) was performed by my labmate and PhD student Jagadish Vemula, and his results are presented in Figure 5.2 for justifying the use of a 490x240 grid for this problem. Further, the plot of wall pressures at three locations along the spanwise directions (Figure 5.3) shows that 5 cells along each z axes is sufficient to ensure two dimensionality of the flow. (z=1,3 and 5 refer to the cell numbers and not distance; with z =1 being the location at the midplane)

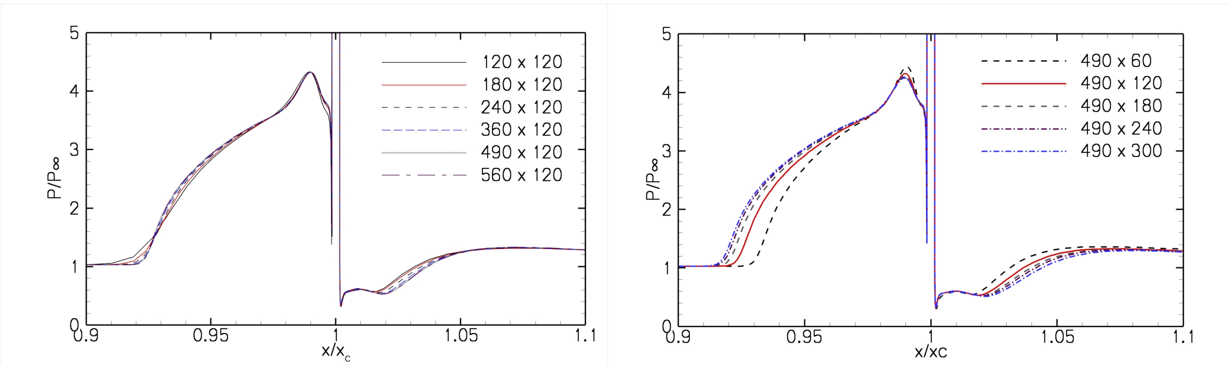

(a) Grid convergence along X axis

(b) Grid convergence along Y axis

Figure 5.2: Grid convergence results of Jagadish Vemula

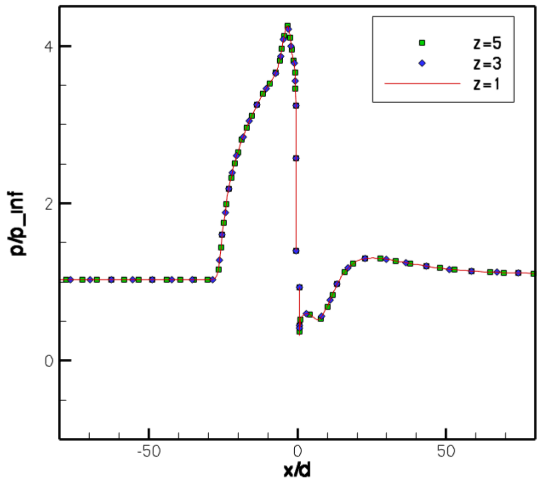

Figure 5.3: Check for two-dimensionality of flow - wall pressure ratios along different span-wise locations

5.3 Arriving at Convergence

The Courant-Friedrichs-Lewy (CFL) condition is a necessary condition for convergence while solving hyperbolic PDEs numerically. There is a limit to the time step that can be taken for converging to a steady solution. This limit is defined by the maximum CFL number a solver can handle.The time step taken for iterations is determined from the CFL number that we are using, as shown in Equation 5.5.

$$CFL = \frac{(u + a)\delta t}{\delta x} < CFL_{max} \tag{5.5}$$

Where,
$u + a$ = maximum speed obtained from eigen values
δt = time step of the iterations
δx = is the minimum grid size, it changes locally from grid to grid. A larger CFL number means a larger δt of time marching, which means that we reach our steady state solution faster. For explicit schemes, the value of CFL is limited below unity, because above it, the results start diverging. An implicit scheme allows the use of higher CFL values. Initially, when the flow is still developing, low values of CFL were used. The value was gradually increased as the flow began developing. Care must be taken that there are no sudden jumps in the CFL values while the flow is still at a sensitive stage of development. The convergence is checked by keeping track of the residual. The residual is calculated with respect to the density as follows -

$$\epsilon = RMS(\rho^{n+1} - \rho^{n}) \tag{5.6}$$

It is the root mean square of the change in density from one iteration to the next. Table 5.5 shows the values of CFL used over a range of iterations and the corresponding drop in residual. Note that the intermediate values of CFL are not mentioned, it does not mean that the CFL jumps took place only at the mentioned iteration numbers.

Table 5.5: CFL and residual variation during iterations

Iteration	CFL used	Residual (local)
200	1	4.0E+3
500	3	7.0E+2
1000	15	1.4E+2
2000	100	3.7E+1
4000	500	9.6E+0
8000	1000	1.4E+0
10000	1100	2.9E -1
13000	1150	1.1E -1
16000	1275	3.0E -2
23000	1100	6.0E -4

It is clear from Table 5.5 that atleast 5 orders of residual drop was obtained over 16000 iterations. Further, the wall pressure ratio and skin friction coefficient are plotted (see Figure 5.4) in order to check for convergence. We may conclude that 16000 iterations on the standard model are enough to give a reasonably converged solution.

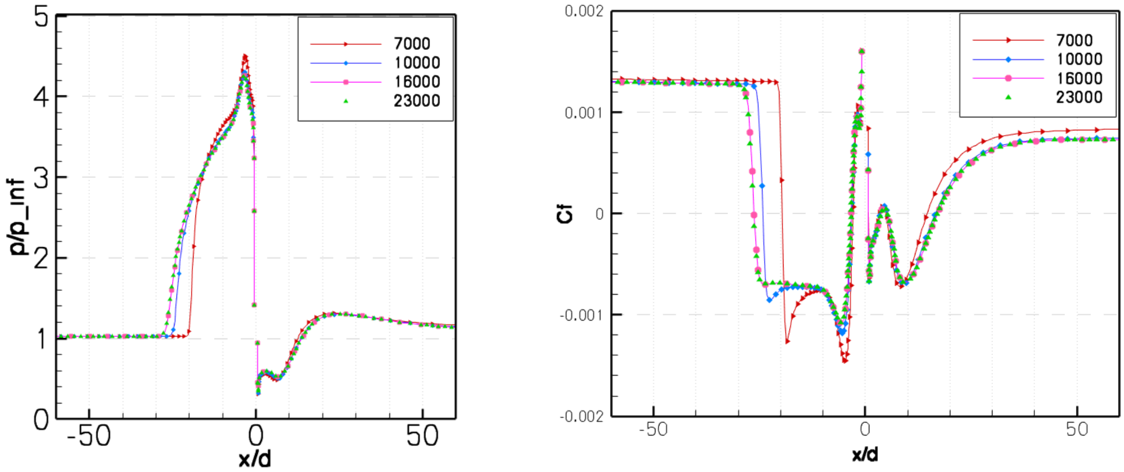

(a) Static wall pressure ratio plot after n iterations

(b) Plot of skin friction coefficient after n iterations

Figure 5.4: Check for convergence

5.4 Results - Standard Model

5.4.1 Contours and Plots at NPR 17.7

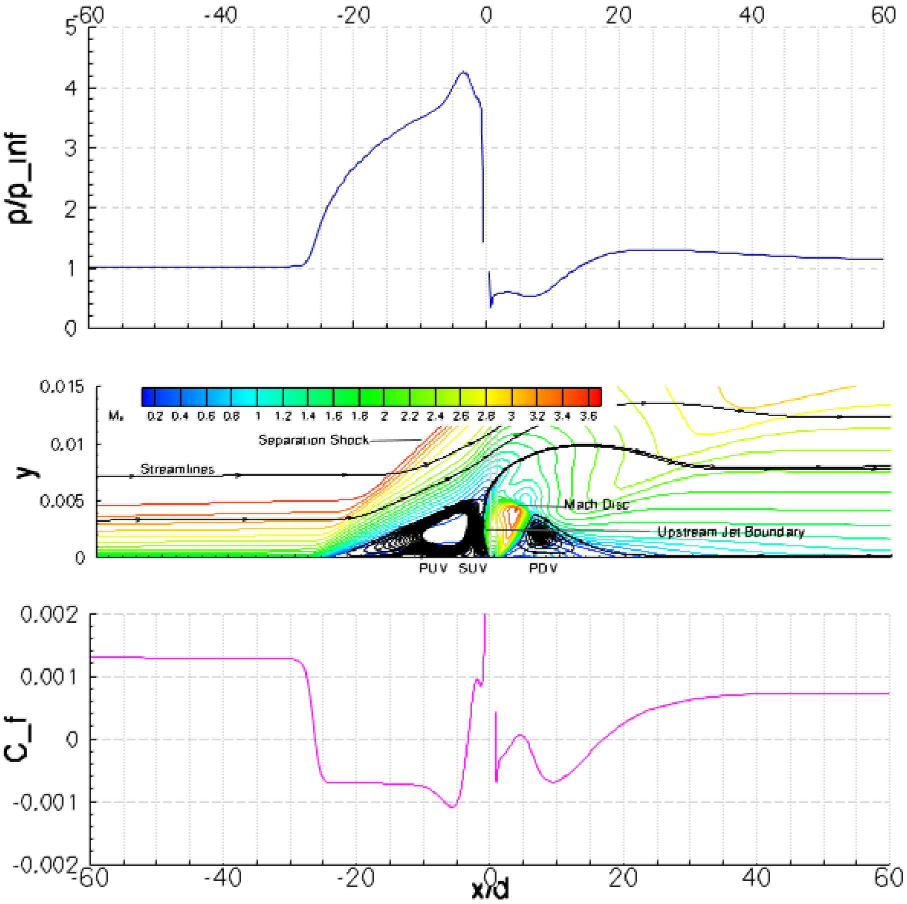

Figure 5.5: Results - Wall pressure, Mach contour, Skin friction coefficient

The Mach contours of the results are shown in Figure 5.5. The Mach disc is clearly seen, as well as the upstream bow shock and separation shock. The subsonic recirculation region is also seen. This contour can be compared to Figure 1.2. The pressure rise is superimposed with the flow field in Figure 5.5. The sharp initial pressure rise is due to a separation shock. It is followed by a gradual plateau; this is the region of the primary upstream vortex. Next, another peak is seen in the wall static pressure, this is where the secondary upstream vortex begins. As predicted, the pressures downstream of the jet are low. The downstream pressure rises when the reattachment shock is encountered. Interestingly, the secondary downstream vortex is almost absent.

5.4.2 Comparison of all NPR Simulations with Experimental Data

The experiments of Aso et al.[3] had cases with several different jet injection pressures. After obtaining results for the NPR 17.7 case, the same code was run with four different jet injection pressures (specified in Table 5.2). The normal wall pressure distribution has been compared with the experimental data and shown in Figure 5.6.

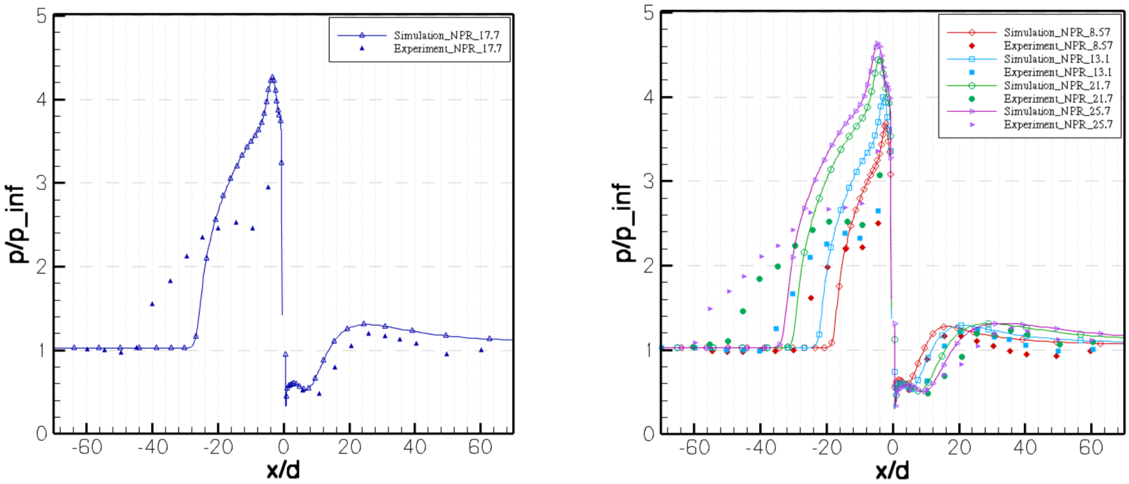

(a) NPR 17.7 (b) Other NPRs

Figure 5.6: Wall pressure distribution compared with experimental data

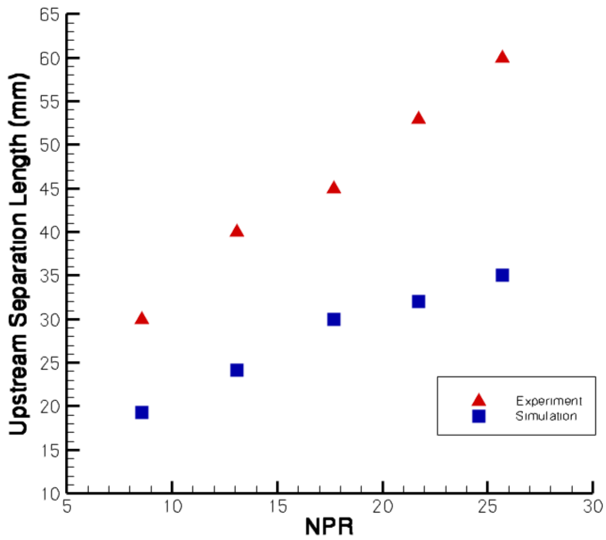

Figure 5.7: Impact of NPR on upstream separation length

The following points are noted -

1. For the NPR 17.7 case, the separation length is highly underpredicted by our model, 40 % less than the actual length. Recorded peak pressures are 45 % greater than experimental values. Downstream pressure distribution also has slight errors.
2. As seen in Figure 5.7, a higher NPR creates earlier separation. This is due to stronger shocks and a higher adverse pressure gradient on the boundary layer.
3. Further, the error in prediction of separation length increases at higher injection pressures. This is possibly because the shocks are stronger and the standard model fails to capture the true physics of the shock turbulence interaction for such cases. Thus, in order to improve our model, we proceed to implement the SU modification to the standard $k-\omega$ model.
4. Although the current model is unable to predict the static pressures with a quantitative accuracy, there is a reasonable about of qualitative matching with the results of the experiments.

5.5 Results - Shock Unsteadiness Modification

5.5.1 SU 2005 Correction

As explained in Chapter 4, the effects of shock unsteadiness in turbulence is taken into consideration by modifying the production term P_k of turbulent kinetic energy k. The convergence of results is seen in Figure 5.8. Unlike the simulations run with the standard model which ran for 16000 iterations, this case was run for 23000 iterations. The shock damping parameter $b_1^{'}$ was initially 0.28. It was then varied to 0.1,0.2 and 0.4. The results are shown in in Figure 5.9. Further the Shock Function (f_s) contour with $b_1^{'}$ = 0.28 is shown in Figure 5.10. The contour was almost same for other values of $b_1^{'}$ too. Following points are noted -

1. The upstream separation length slightly increases due to the impact of the Shock Unsteadiness Modification. However, peak pressures remain same as that predicted by standard model.
2. There isn't any noticeable effect of varying the shock damping parameter.
3. The f_s contour doesn't accurately capture the shape of the upstream shocks.

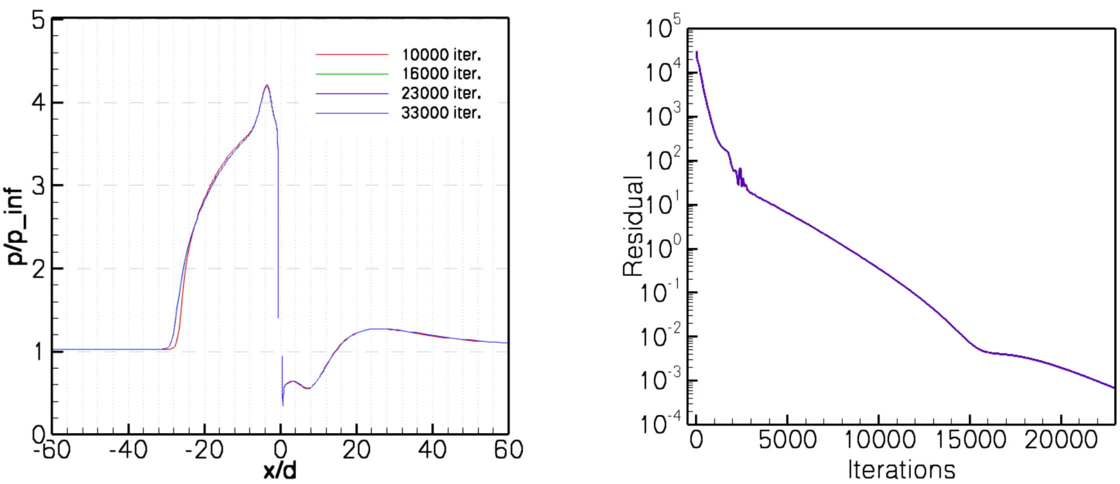

(a) Convergence of wall pressure ratio plot

(b) Residual drop over 23000 iterations

Figure 5.8: Convergence with 2005 SU model

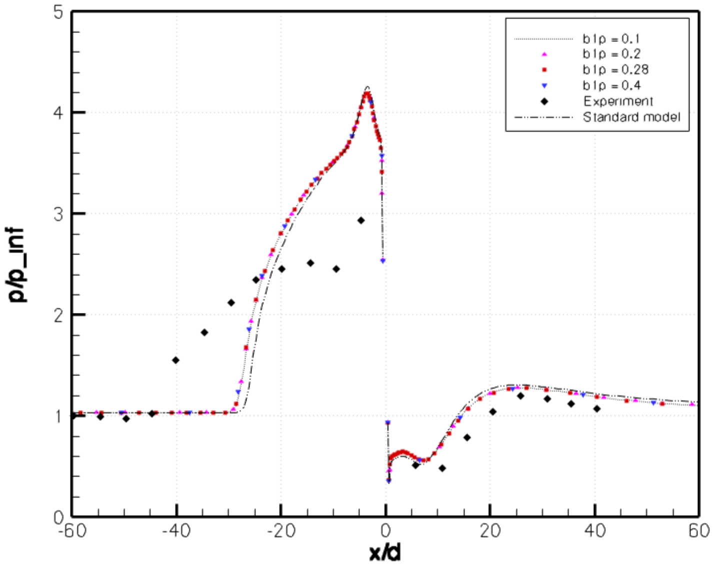

Figure 5.9: Wall pressure ratio plots - comparing 2005 model with standard model and experimental data

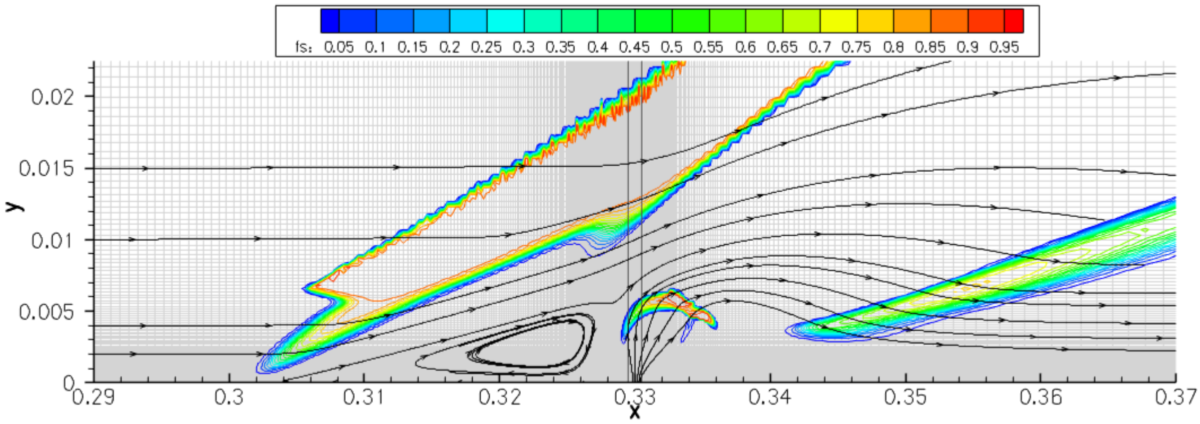

Figure 5.10: Shock function contour for 2005 SU model ($b_1^{'}$ = 0.28)

5.5.2 SU 2008 Correction

Since the SU 2005 model could not capture the shocks properly, the SU 2008 model was given a go. Like the SU 2005 model, all results given here converge after 23000 iterations. Two values of $b_1^{'}$ (0.1 and 0.4) are taken for comparison. The results are shown in Figure 5.11 and compared with the previous models.

The following behaviour is observed -

1. There is significant improvement in the capturing the upstream separation location. **The error in its prediction is now 20% lesser than the error arising from the standard $k - \omega$ model.** The peak pressures show considerable improvement too.
2. The 2008 SU Model is more sensitive to the variation of $b_1^{'}$ as compared to the 2005 Model. A higher value of shock damping results in earlier separation of the boundary layer. This is consistent with the physics behind the Shock Unsteadiness Model. Although, like the case with 2005 model, there isn't much effect of $b_1^{'}$ on the peak pressures.
3. The 2008 shock function is able to capture the shocks well. This is seen in Figure 5.12

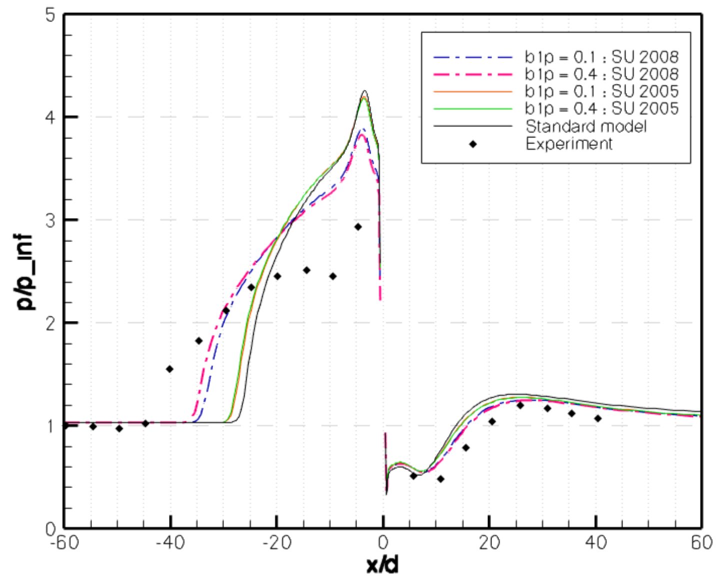

Figure 5.11: Wall pressure ratio plot for 2008 SU model ($b_1^{'}$ = 0.1 and 0.4), compared with previous models

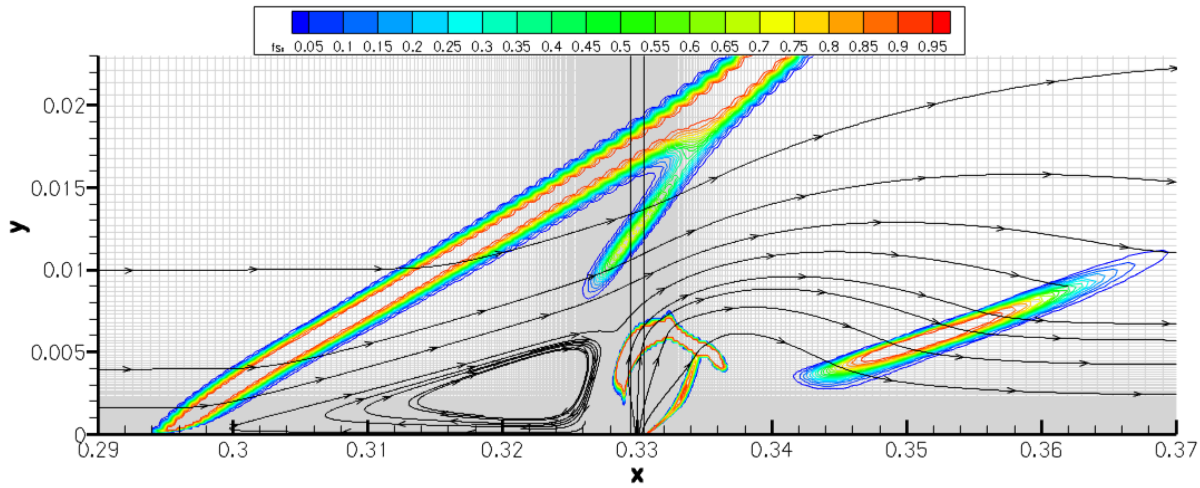

Figure 5.12: Shock function contour for 2008 SU model ($b_1^{'}$ = 0.4)

5.5.3 Altering SU 2008 Equation

Until now, we have presented results which came from models available in literature. An attempt was made to modify some parameters in the original SU 2008 equation such that-

$$f_s = \frac{1}{2} - \frac{1}{2} tanh\left[a * (S_{ii}\delta_0/U_\infty) + b\right] \tag{5.7}$$

where variables a and b have replaced the coefficients 4 and 12 of Equation 4.9 . In order to study the impact, first a is held constant at 12 and b is varied to 3 and 5. Then, b is held constant at 4 and a is varied to 20 and 7. The effect of these changes is shown in this section. The value of δ_0 = 0.0056 and U_∞ = 665 m/s.

From the f_s contours in Figure 5.13 we understand that a larger value of a amplifies the regions of compression, leading to thicker shocks and earlier separation. Whereas, a larger value of b results in more region of zero f_s, resulting in thinner shocks closer to injector.

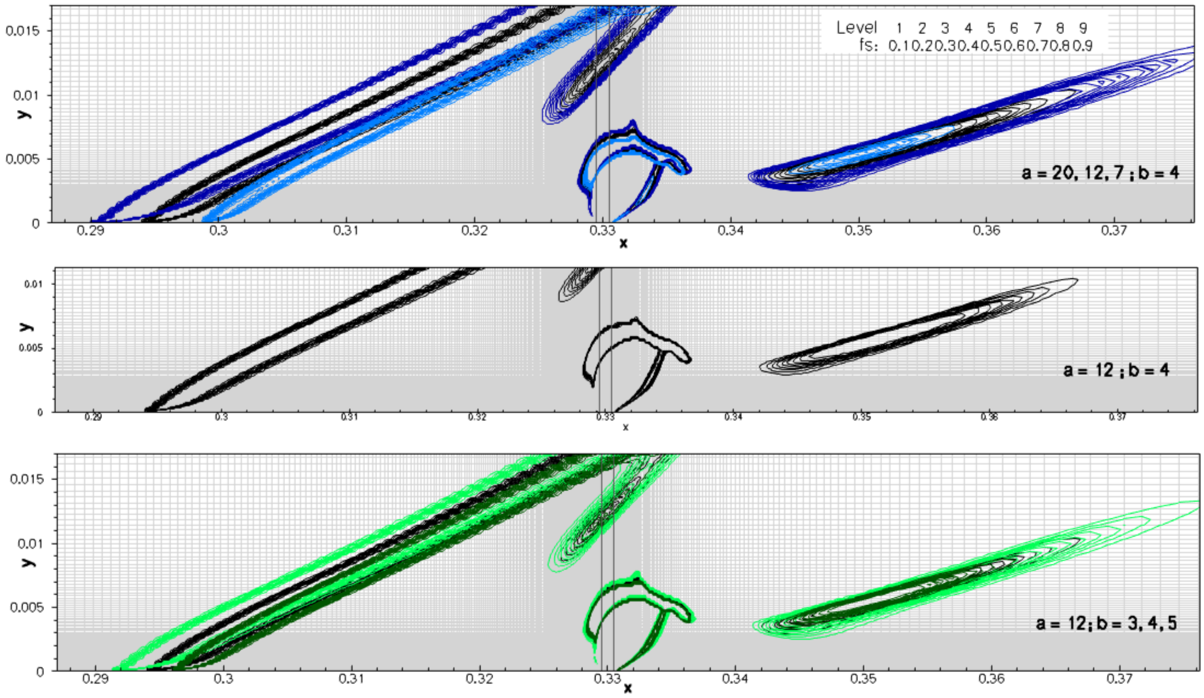

Figure 5.13: Effect of changing variables a and b on shock function contours (lighter shade = lower value)

Since f_s is a function of S_{ii}, we take our SU 2008 result and check the values of S_{ii} at the shock wave. (See contour of Mach and S_{ii} (div) in Figure 5.14a). We see that our shock is located within a region where S_{ii} is 30,000-60,000. We term this range of S_{ii} as our region of interest. Next, we plot f_s vs S_{ii} at several combinations of a and b (Figure 5.14b).

Our aim is to have an f_s distribution such that it has values close to one in our region of interest and zero for regions of lower compression. A value of **a = 12 and b = 3** serves this purpose well. We run a simulation using these values of a and b; and the results are presented in Figure 5.15.

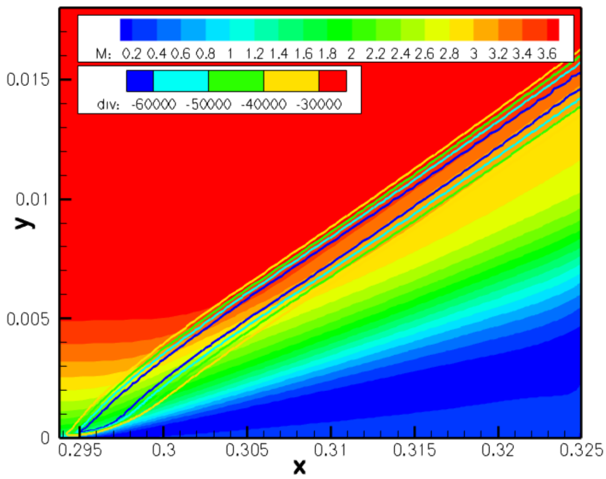

(a) S_{ii} line contour superimposed over mach contour (SU 2008)

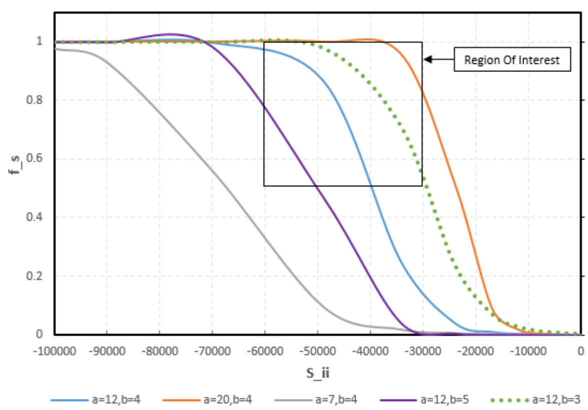

(b) f_s vs S_{ii} at different a,b

Figure 5.14: Selecting values for a and b

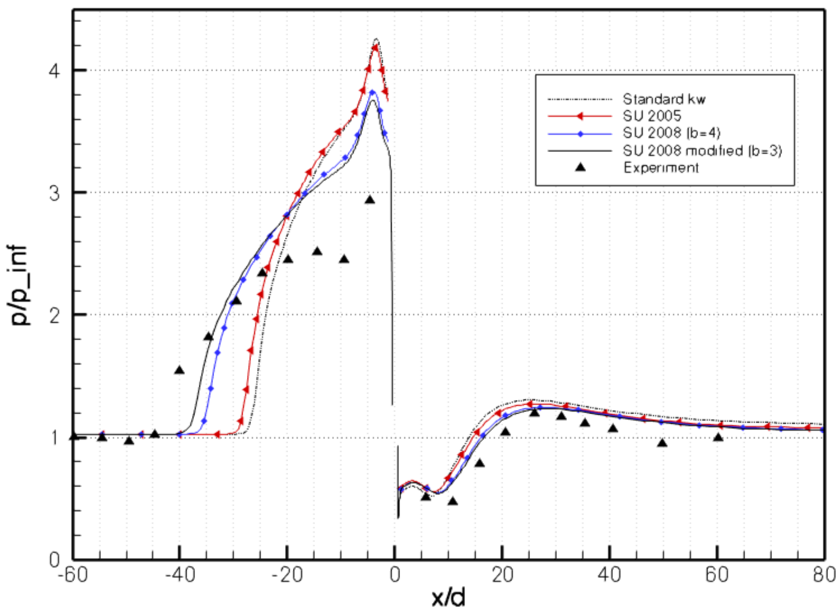

Figure 5.15: Comparing the modified SU 2008 model with standard,SU 2005,SU 2008 and experimental results

In order to quantify the impact of the modified version on the upstream separation point location, we plot (Figure 5.16) the variation of C_f for our models - the point where C_f goes from positive to negative indicates separation. The experiment[3] suggested separation at -44 *mm*. The error w.r.t the experiment associated with our models is shown in Table 5.6.

Table 5.6: Improvement obtained in prediction of upstream separation point

		Standard $k-\omega$	SU 2005	SU 2008	Modified SU 2008
X_{sep}	mm	-26.22	-27.98	-34.59	-36.87
Error	%	40	36	21	16

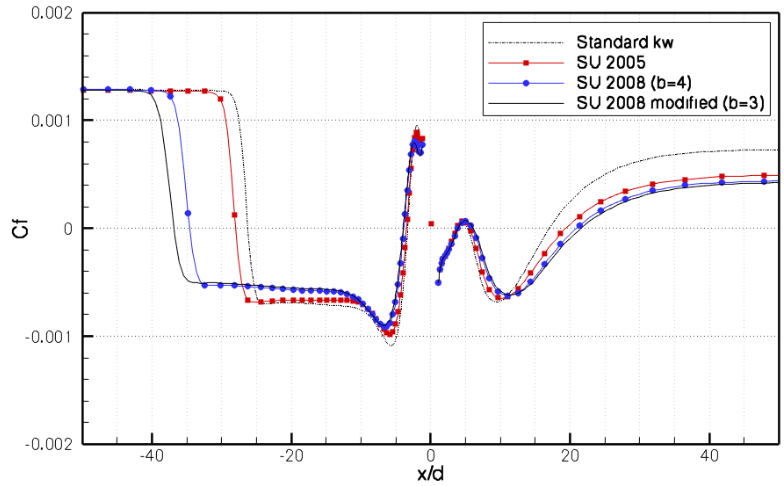

Figure 5.16: C_f plots of simulations for locating the separation point

5.6 Comparison with Previous Simulations and Experiment

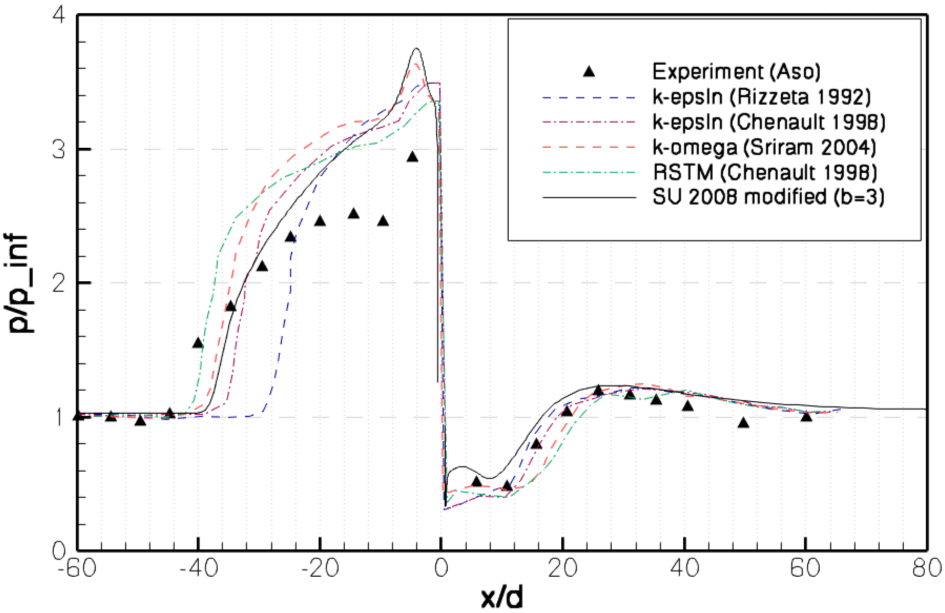

Figure 5.17: Plot of modified SU 2008 model (b=3) compared with experimental data[3] and past simulations[20,21,4]

We observe the following points -

1. Our results compare well with the k-ω model of Sriram and Mathew[4] - even though they used a higher order scheme and compressibility correction.
2. Our model captures the upstream separation more accurately than the k-ϵ simulation of Chenault and Beran[21] but not as well as their RSTM results.
3. There is scope for improvement in prediction of the peak pressure.
4. Our model matches the pressure plateau region more closely than any of the other models.

5.7 Summary

The flow conditions, boundary conditions, grid details, and convergence was explained; following which results were presented for Aso's NPR 17.7 jet injection case using a standard k-ω model. Simulations at other NPR cases were also run and the trend in the location of upstream separation point was highlighted. Next, in order to improve the standard model, the Shock Unsteadiness model[1] was incorporated in two forms (2005 and 2008 version[24,25]). The SU 2008 version was further altered by changing variables in its f_s equation. A good amount of improvement in upstream separation length was achieved with each successive SU modification.

Chapter 6

Summary and Scope

6.1 Summary

1. Chapter 1 introduced us to the flow field arising from transverse injection of an underexpanded sonic jet into a supersonic cross-flow. The flow features arising from such an injection were studied in the two dimensional as well as three dimensional scenarios.
2. The previous experimental and simulation results of the flow field for the two dimensional slot injection cases have been reviewed in Chapter 2. Some review of the three dimensional case has also been done. Important parameters such as momentum flux ratio have been defined.
3. In Chapter 3 , the basic physics of the flow field has been expressed mathematically through governing Navier Stokes Equations. Numerical concepts such as discretisation methods and Steger Warming scheme were explained. We implement the $k-\omega$ model, but the uses and significance of other turbulence models is also discussed briefly.
4. With strong shock-turbulent interaction, the standard $k-\omega$ is incapable of accurately capturing the flow physics. Chapter 4 elucidates the Shock Unsteadiness Modification that helps improve the standard model. The important variables and functions ($b_1^{'}$ and f_s) are highlighted, and the various versions of the SU Models are presented.
5. Chapter 5 presents the simulations that have been carried out for a two dimensional injection case of the experiments of Aso et al.[3] The pre-processing of the simulations is explained. Results are obtained for
   - Standard $k-\omega$ model
   - 2005 SU $k-\omega$ model
   - 2008 SU $k-\omega$ model
   - 2008 SU $k-\omega$ model with modified f_s equation.

   The results are compared with data available in literature. Attempt has been made to accurately capture the upstream separation location using several forms of the shock unsteadiness model and the error in its prediction is compared. **A reduction of error from 40% to 16% is obtained by using a modified SU 2008 model over the standard k-ω model.**

6.2 Future Work

1. Higher order simulations for the current case are under-way. Once those results are obtained, we can judge the model more accurately .
2. Next, SU simulations can be run at different pressure ratios for which experimental data is available, following which trends can be observed.
3. Finally, three dimensional jet injection cases can be simulated and studied with the standard and SU models.

Bibliography

[1] Sinha, K., Mahesh K., and Candler, G.V., "Modeling shock unsteadiness in shock/turbulence interaction." Physics of Fluids (1994-present) 15, no. 8 (2003): 2290-2297.

[2] Aso, S., Okuyama, S., Kawai, M., and Ando, Y. Experimental study on the mixing phenomena in supersonic flows with slot injection. AIAA Paper 91-0016, 1991.

[3] Aso, Shigeru, Satoshi Okuyama, Yasunori Ando, and Toshiro Fujimori. "Two-dimensional and three-dimensional mixing flow fields in supersonic flow induced by injected secondary flows through traverse slot andcircular nozzle." In 31st Aerospace Sciences Meeting, p. 489. 1993.

[4] Sriram, Atheya, and Joseph Mathew. "Numerical prediction of two-dimensional transverse injection flows." In 42nd AIAA Aerospace Sciences Meeting and Exhibit, p. 1099. 2004.

[5] Sriram, A. T., and Joseph Mathew. "Improved prediction of plane transverse jets in supersonic crossflows." AIAA journal 44, no. 2 (2006): 405-408.

[6] Sriram, A. T., and Joseph Mathew. "Numerical simulation of transverse injection of circular jets into turbulent supersonic streams." Journal of Propulsion and Power 24, no. 1 (2008): 45-54.

[7] Subhajit Roy, Turbulent Heat Flux modeling for high speed flows. PhD second annual progress report, IIT Bombay, 2017.

[8] Steger, Joseph L., and R. F. Warming. "Flux vector splitting of the inviscid gasdynamic equations with application to finite-difference methods." Journal of computational physics 40, no. 2 (1981): 263-293.

[9] Wright, Michael James. "A family of data-parallel relaxation methods for the Navier-Stokes equations." (1997).

[10] Amick J. L., and N. E. Hawk. "Two-dimensional secondary jet interaction with a supersonic stream." AIAA Journal 5, no. 4 (1967): 655-660.

[11] Spaid, F. W., and E. Zukoski. "Secondary injection of gases into a supersonic flow." AIAA journal 2, no. 10 (1964): 1689-1696.

[12] Spaid, F. W., and E. E. Zukoski. "A study of the interaction of gaseous jets from transverse slots with supersonic external flows." AIAA journal 6, no. 2 (1968): 205-212.

[13] Morkovin, Mark Vladimir, C. A. Pierce Jr, and C. E. Craven. Interaction of a side jet with a supersonic main stream. No. UM-N-11701. Michigan University, Ann Arbor, Engineering Research Institute, 1952.

[14] Hawkins, P. F., H. Lehman, and J. A. Schetz. "Structure of highly underexpanded transverse jets in a supersonic stream." AIAA journal 5, no. 5 (1967): 882-884.

[15] Billig, F. S., and J. A. Schetz. "Penetration of gaseous jets injected into a supersonic stream." Journal of Spacecraft and Rockets 3, no. 11 (1966): 1658-1665.

[16] Gruber, M. R., A. S. Nejadt, T. H. Chen, and J. Craig Dutton. "Mixing and penetration studies of sonic jets in a Mach 2 freestream." Journal of Propulsion and Power 11, no. 2 (1995): 315-323.

[17] Santiago, Juan Gabriel, and J. Craig Dutton. "Velocity measurements of a jet injected into a supersonic crossflow." Journal of Propulsion and Power 13, no. 2 (1997): 264-273.

[18] Everett, D. E., M. A. Woodmansee, J. Craig Dutton, and M. J. Morris. "Wall pressure measurements for a sonic jet injected transversely into a supersonic crossflow." Journal of Propulsion and Power 14, no. 6 (1998): 861-868.

[19] Nithiyaraj Munuswamy, Jet injection into supersonic crossflow: Flowfield and mixing studies. PhD Thesis, IISc Bangalore, 2018.

[20] Rizzetta, D. P. "Numerical simulation of slot injection into turbulent supersonic supersonic stream". AIAA J. Vol. 30, No. 10 , 1992, 2434-2439.

[21] Chenault, C., and Beran, P. S. "k-w and Reynolds stress turbulence model comparisons for two-dimensional flows". AIAA J. Vol. 36, No.8, 1998, 1401-1412.

[22] Gerlinger, P., Algermissen, J., and Bruggemann, D. "Numerical simulation of mixing for turbulent slot injection". AIAA J. Vol. 34, No. 1, 1996, 73-8.

[23] Champigny, P., and Lacau. R. G. "Lateral jet control for tactical missiles." ONERA (1994).

[24] Sinha, K., Mahesh K., and Candler, G.V., "Modeling the effect of shock unsteadiness in shock/turbulent boundary-layer interactions." AIAA journal 43, no. 3 (2005): 586-594.

[25] Pasha, A.A., and Sinha K. "Shock-unsteadiness model applied to oblique shockwave/turbulent boundary-layer interaction." International Journal of Computational Fluid Dynamics 22, no. 8 (2008): 569-582.

[26] Pasha, A.A., and Sinha, K., "Simulation of hypersonic shock/turbulent boundary-layer interactions using shock-unsteadiness model." Journal of Propulsion and Power 28, no. 1 (2012):46-60.